Thesis for the Degree of Doctor of Philosophy
In
Thermo and fluid Dynamics

Predictions of Aerodynamically Induced Wind Noise Around Ground Vehicles

Jonas Ask

Division of Fluid Dynamics

Department of Applied Mechanics

Chalmers University of Technology

Göteborg, Sweden, 2008

Predictions of Aerodynamically Induced Wind Noise Around Ground Vehicles

Jonas Ask
ISBN 978-91-7385-081-0

Doktorsavhandling vid Chalmers tekniska högskola
Ny serie nr 27622762
ISSN 0346-718x

Division of Fluid Dynamics
Department of Applied Mechanics
Chalmers University of Technology
SE-412 96 Göteborg
Sweden
Phone +46-(0)31-7721000

This document was typeset using LaTeX

Printed by Chalmers Reproservice
Göteborg, Sweden 2008

Predictions of Aerodynamically Induced Wind Noise Around Ground Vehicles

Jonas Ask

Division of Fluid Dynamics
Department of Applied Mechanics
Chalmers University of Technology

Abstract

Over the last decade wind noise has with few exceptions consistently generated a constant or even growing level of customer complaints to automotive companies worldwide. This can partly be explained by a relatively greater focus on engine, power-train and tire noise combined with a growing need to reduce weight in future cars.

One class of wind noise problems commonly referred to as *air-rush noise* relates to turbulent pressure fluctuations caused by separated or vortical flows, which is addressed in this thesis.

Sound generation and to some extent sound propagation are here evaluated from incompressible flow fields, since the unsteady flow hydrodynamics at low Mach numbers is often the dominant source of sound. A temporal form of Curle's equation is used in these evaluations. It is shown that the noise level measured inside the compartment of a production vehicle has a dipole character. Accordingly, sound generation is evaluated from the dipole terms in the acoustic analogy and, for one specific case, the radiated sound is evaluated by the surface integral of the same terms.

Three different cases are investigated, ranging from the laminar flow past an open two-dimensional cavity to the turbulent flow past a representative ground vehicle. It is shown that the dipole terms in Curle's equation can with sufficient accuracy be predicted for the regions of interest even for the full vehicle case. A potential problem is highlighted, which is that, even if the acoustic source magnitudes are correctly predicted in an incompressible field, the sound directivity may be erroneous due to distortions in the pressure field and small differences in the flow field for flows with few but dominant structures.

Keywords: CAA, LES, Curle, low Mach number, incompressibility, air rush noise, cavity, side mirror, ground vehicle

List of Publications

This thesis is based on four papers:

1. Ask, J., Davidson, L., An acoustic analogy applied to the laminar upstream flow over an open cavity, C.R. Mecanique, Vol 333(2005), pp. 660-665

2. Ask, J., Davidson, L., Sound generation and radiation of an open 2-D cavity oscillating in wake mode, submitted to AIAA Journal, (2007)

3. Ask, J., Davidson, L., A numerical investigation of the flow past a generic side mirror and its impact on sound generation, submitted to JFE, (2007)

4. Ask, J., Davidson, L., Flow and dipole source evaluation of a generic SUV, submitted to JFE, (2007)

Division of work between the authors of the papers

This thesis is based on the four papers listed above. The present author is the first author of all the papers in this thesis and produced all the results except for the reference simulations in papers (1) and (2) and the measurements in paper (3) given in the publication list. The theoretical results in all the papers were discussed with the supervisor, Professor Lars Davidson.

Other Relevant Publications

Ask, J. 2005, A study of incompressible flow fields for computational aero acoustics, Thesis for Licentiate of Engineering. Department of Applied Mechanics, Chalmers University of Technology, Göteborg, Sweden

Ask, J. & Davidson, L. 2005, An investigation of outlet boundary conditions for incompressible near field acoustics, 11th AIAA/CEAS Aeroacoustics Conference, AIAA-2005-2992, 23-25 May, Monterey, California

Ask, J. & Davidson, L. 2006, The sub-critical flow past a generic side mirror and its impact on sound generation and propagation, 12th AIAA/CEAS Aeroacoustics Conference, AIAA-2006-2558, 8-10 May, Cambridge, Massachusetts

Acknowledgments

This work was carried out at the Division of Fluid Dynamics at Chalmers University of Technology and at the Environment and Fluid Dynamics Department at Volvo Car Corporation. The project was funded by the Volvo Car Corporation and VINNOVA.

I would first like to thank my former manager, Dr. Magnus Olsson at Volvo Car Corporation, who gave me this opportunity and for recurrent reminders of how few things an open cavity and a car have in common. I would also like to express my deepest gratitude to my supervisor, Professor Lars Davidson, for always being encouraging, open minded and questioning things not fully understood.

To the two persons who guided my first trembling steps in the field called aero acoustics, Dr. Johan Larsson and Dr. Mattias Billson, thank you for taking your time. Thanks also to Dr. Niklas Andersson for sharing ideas and experiences as well as for being a great travel companion during the conferences.

Thanks also to my former industrial supervisor and manager, Dr. Hans Enwald, for support with the perhaps most difficult part, namely the project administration.

To my former colleague Dr. Andreas Borg, thanks for your advice during this time. Without it I believe I would have spent all my time on boundary conditions.

Thanks also to FLUENT Sweden and particularly to Dr. Fredrik Carlsson for support with the code.

Thanks to all my other colleagues at Volvo for a joyful time and help during this time.

Last but not least, thanks to my wife Camilla for her support and making my ordinary life function.

Nomenclature

Geometric quantities

x_i	Cartesian tensor coordinate
y_i	Cartesian tensor coordinate of source location
$\mathbf{x}$	observation coordinates
$\mathbf{y}$	source coordinates
D	depth
H	height
L	length or integral scale
r	distance from source to observer
n_i	unit surface normal pointing towards fluid
l_i	unit vector pointing from source to observer

Roman letters

N_{xyz}	number of grid points
U_∞	freestream velocity
u	velocity scale
x_1	streamwise coordinate
x_2	lateral coordinate

Greek Symbols

α	calibration constant
β	calibration constant
σ	buffer parameter
λ	acoustic length scale
ω	vorticity
ν	kinematic viscosity
η	Kolmogorov length scale
ρ	density
τ_{ij}	viscous stress tensor
δ_{ij}	Kronecker delta
τ	retarded time
Δ	LES length scale

Flow quantities

a	speed of sound
p	pressure

Various quantities

$\widetilde{l}$	length scale
d_w	wall distance
u_i	instantaneous velocity
T_{ij}	Lighthill's tensor
f	frequency
t	time
I_ω	vortex strength

Dimensionless quantities

C_{DES}	model constant
Re	Reynolds number
Ma	Mach number
n^+	wall unit, normal direction
l^+	wall unit, lateral direction
s^+	wall unit, spanwise direction
C_p	pressure coefficient (or specific heat)

Math symbols

$\|f\|$	magnitude
$\dot{f}$	temporal derivative
$[f]$	retarded time

Subscripts

0	reference condition
∞	ambient state
$init$	initial condition
m	monopole
d	dipole
q	quadrupole
rms	Root Mean Square
t	turbulent condition, or tangential

Superscripts

$'$	fluctuation

Abbreviations

BLE	Boundary Layer Equation
DES	Detached Eddy Simulation
DNS	Direct Numerical Simulation
DS	Direct Simulation
FVM	Finite Volume Method
$GQRS$	Global Quality Research System
$HVAC$	Heating, Ventilating and Air Conditioning
LBM	Lattice Boltzmann Method
LNS	Limited Numerical Scale
LES	Large Eddy Simulation
$OASPL$	Over All Sound Pressure Level
$RANS$	Reynolds Averaged Navier Stokes
SPL	Sound Pressure Level
SGS	Sub-Grid Scale
$URANS$	Unsteady Reynolds Averaged Navier Stokes

Contents

Chapter 1

Objectives and overall goals

The research hypotheses in the present work are as follows:

1. Is the assumption of incompressibility justified for low Mach number, wall-bounded flows where the hydrodynamics is the dominating cause of noise generation?
2. Do the surface pressure terms provide sufficient information to evaluate the emitted sound in a representative vehicle where air-rush noise is our main concern?
3. Can a method be established to at least qualitatively predict air-rush noise for a production vehicle fulfilling industrial needs of both robustness and accuracy?

Aside from testing these hypotheses, the research aims to:

4. Give relevant guidelines for industry regarding numerical schemes, turbulence models and spatial resolution with respect to capturing the acoustic sources.

Chapter 2

Introduction

The only legal restriction on noise emissions for car manufacturers in Sweden concerns *by-pass noise* measured during full acceleration along a 25-meter road strip 7.5 meters from the center plane of the car. During this test a common passenger car reaches a top speed of about $50-70$ [km/h]. Under these conditions, the flow-induced noise is negligible as compared to noise caused by the engine, power-train and road-tire interaction. The chief motivation for reducing flow-induced noise in future cars thus concerns the driver's and the passenger's subjective experience.

Up to the last decade car customers have fortunately shown a high tolerance for this type of noise, which is one of the main noise sources under cruising conditions. The explanation has been a noise level more or less independent of brand and car generation. The customer has been "taught" that these noise levels are to be expected in every car, and complaints have been raised only when the level was so high that the passengers were unable to hear conversation or the radio, see Thomson [1]. This trend has shifted in the last decade. Several automotive companies have invested in acoustic wind tunnels and research aiming at find the cause of noise levels and to reduce them in modern cars. Customer surveys such as GQRS and JD Powers give indications that a handful of those companies have almost halved their number of customer complaints during the last ten years while the other companies have stayed at a constant level or even recieved a greater number of customer complaints. Still, ten years may not be a sufficiently long timespan to study the effect of the investments made. It is therefore most probable that the remaining companies that have a clear ambition to solve the problem may

join the more successful companies within a few years. A secondary effect might also be that customers who have driven or owned a more "silent" car in the premium segment will probably show less acceptance of a more "noisy" car, which suggests that the spread in complaints will even increase in the future if no actions are taken.

Flow-induced noise in ground vehicles is here defined as the undesirable noise experienced by the driver or passengers caused by internal or external flows. A reduction of and knowledge about the underlying mechanisms of this noise generation and radiation to the driver or passengers thus represents a research field of great importance to the world's automotive companies.

In 1971, Stapleford and Carr [2] divided flow-induced noise into three main categories:

- Unpitched noise caused by air rushing past the vehicle exterior
- Monotone noise casued by sharp edges and gaps on the exterior of the vehicle
- Acoustic resonance directly influencing the compartment noise level caused by flow excitation of openings in the vehicle, such as side windows and sunroofs.

The *exterior* will in the following text refer to surfaces with a surface normal pointing away from the vehicle. In contrast, the *compartment* is the restricted volume in which the driver and passengers are located.

The first category in the list is typically unpitched or broadbanded in character and is commonly referred in the literature to as *air-rush noise* or *wind noise*. This noise is commonly expected to dominate over other noise sources at speeds above $100 - 160$ [km/h] if leakages are prevented. Romberg and Lajoie [3] showed in 1977 that the wind noise becomes the most dominant source at cruising speeds at about 145 [km/h], for a typical car of that date. In 1983, Buchheim et al. [4] showed that, at a speed of about 160 [km/h], wind noise becomes as important as all other sources by comparing wind tunnel tests with on-road tests. Since then, noise generated by engines , power-train and to some extent road-tire interaction has been significantly reduced, particularly in cars in the premium segment. George [5] reported in 1990 that cars in the this segment are significantly affected by wind noise at speeds in the order of 100 [km/h].

If the air-rush noise relates only to unpitched noise, there must be flow phenomena that can give rise to tonal noise. Stapleford and Carr [2] claimed that pitched noise is mainly due to sharp edges and gaps or cavities, which involve different flow physics as compared to air-rush noise. For example, a cavity can give rise to self-sustained flow oscillations creating a tonal noise under certain conditions. The speed at which these oscillations occur is not as distinct as for air-rush noise but is closely related to the cavity or edge dimensions and the local boundary layer thickness. Pitched noise can also occur from the transition from laminar to turbulent boundary layers, although it is not mentioned in the above list. This is typically the case for side view mirrors and has been reported, for example, by Lounsberry et al. [6].

Flow-induced noise can however be the overall dominant component in the car compartment at lower speeds. This is typically the case in the presence of open windows and sunroofs, which are often referred to in the literature as *buffeting* or *wind-throb* noise. This is a resonance phenomenon that is strongly dependent on the compressibility of the fluid, typically occurs in the range between 40 and 100 [km/h] and can generate more than 120 [dB] inside the compartment.

Another noise source more prominent at lower flow speeds is the heating, ventilating and air conditioning (HVAC) system. However, the cause and effect in noise levels when the fan speed is increased are better accepted by the driver and are more or less present in all kinds of cars. A remark here is that the driver of a more "silent" vehicle will experience a higher relative change when the HVAC system is active, which can generate more customer complaints than in a "noisier" vehicle. This makes noise reduction a delicate task when isolated systems or components are analyzed.

Returning to the air-rush noise, the level caused by this category of noise that is experienced by the driver or passengers is an effect of two main causes; the first is leakages between the vehicle exterior and compartment, and the second is the aerodynamic shape. Leakage noise, also referred to as *aspiration noise*, is in turn mainly due to unsteady or steady mass flows entering or exiting the vehicle compartment. Shape noise on the other hand enters the compartment mainly through transmission through the vehicle structures that separate the exterior from the compartment.

Depending on its fundamental cause, the aspiration noise may have a different

character. The sound pressure level (SPL) is defined as

$$SPL = 20log_{10}(\frac{p'}{p_0}) \tag{2.1}$$

where p_0 is the reference pressure, $2 \cdot 10^{-5}$ [Pa], and p' is the acoustic pressure fluctuation. Starting with aspiration noise caused by a fluctuating mass flow through a leak in the vehicle exterior, this type of source will have a monopole character and will generally dominate the noise field if present. For a monopole source, the acoustic pressure fluctuation will scale as

$$p'_m \propto u^2 \tag{2.2}$$

where u is a characteristic velocity scale of the source fluctuation. If the leakage is instead steady, it may give rise to a jet-like flow causing pressure fluctuations at the compartment-oriented side of the sealing and turbulence in the free shear layers close to its core. The surface pressure fluctuations will give rise to dipoles which will scale as

$$p'_d \propto Ma \cdot u^2 \tag{2.3}$$

where $Ma = \frac{u}{a_\infty}$ is the turbulent Mach number. If neither monopoles nor dipoles are present, then the noise may have a quadrupole character, caused by turbulence in the free shear layers created by the leakage. This source will scale as

$$p'_q \propto Ma^2 \cdot u^2 \tag{2.4}$$

For low Mach number flows, the quadrupoles will be of less importance, which will be returned to later in the text.

The above mentioned types of sources and their approximations also partly apply for shape noise, since flow separated regions will give rise to both pressure fluctuations at the vehicle exterior and turbulence in the free shear layers, for example downstream of the side mirror. These noise sources will however be generated outside the vehicle and have to be transmitted through the vehicle surface to reach the driver or passengers. It is worth mentioning that leaks can also serve as a path for the shape noise to radiate to the compartment with no significant transmission loss as compared to, for example, the window or door structure. An example is the HVAC system where the transmission loss is generally much lower than in the case of the other surfaces connecting the exterior to the compartment, since it allows noise to

travel relatively unaffected through the ducts when the HVAC is operating in open mode.

In 1964 Thomson [1] conducted road tests to investigate whether aspiration or aerodynamic shape noise is the source that contributes most to wind noise. His study concluded that aerodynamic shape is insignificant compared to air leakages caused by poor seal designs. One argument needed to confirm this conclusion was to identify the effect of cross winds. Cross wind causes both additional pressure changes at the object lee side and larger separation zones, which must be compensated for by proper seals since the aerodynamic shape has a much lesser effect under these conditions. He found that the most critical region was the foremost part of the side windows, the A pillar sealing, followed by the C pillar region close to the beltline and the front door region close to the driver or passenger.

A two part study was initiated by Stapleford and Carr [2, 7] in 1971 to associate different flow regimes with aerodynamic noise levels for generic objects and production vehicles. They found that aerodynamic noise levels were highly associated with different forms of flow separation, particularly from spiral vortex flows present downstream of the A pillar. A direct consequence of this finding was the discovery that aerodynamic shape is an important factor, because minimizing flow separation will help to reduce the wind noise.

Watanabe et al. [8] showed in 1978 that, dipole generated noise was the fundamental cause of wind noise for four cars of that date due to a u^3 scaling of the acoustic pressure. From this finding they concluded that the fundamental cause of wind noise is flow separation. They also identified a relationship between the height of the rain gutter and side window recess depth, which produced the highest noise levels. The air-rush noise was also found to be effectively reduced by decreasing the flow velocity around the A pillar.

Lorea et al. [9] presented a method in 1986 where the aspiration noise could be separated from the shape noise. Their study showed on the one hand that a reduction of the total noise by as much as 6.5 to 9.5 [dB(A)] could be obtained by preventing leakages. The total noise caused by shape noise could on the other hand be reduced by 3 [dB(A)] by just changing to a more aerodynamically shaped side view mirror.

The chain of events from flow separations to pressure fluctuations sensed by the driver or passengers inside the vehicle compartment was investigated by George [5] in 1990. He suggested that dipole generated sound caused by

pressure fluctuations is the most important source of air-rush noise, mainly because the aspiration noise can generally be controlled by known methods. He also discussed an approach for tackling the air rush noise problem based on four steps:

1. Understanding the flow field including the separations
2. Finding the surface pressure fluctuations based on this information
3. Finding the external sound radiation from the pressure fluctuations radiation
4. Finally, finding how these pressure fluctuations transmit through the vehicle structure to generate internal noise.

This short review highlights aspects concerning whether, aspiration and aerodynamic shape is the most dominant source of wind noise in modern cars. The discussion above indicates that both sources are of great importance and, when choosing a suitable predictive method, both aspiration and aerodynamic shape should if possible be taken into consideration. This is possible if the shape noise is evaluated with a knowledge of where eventual leakages are most probable and with efforts to avoid high acoustic source levels in those regions, since there they may generate monopoles and facilitate a short-cut for the external noise to transmit into the compartment.

2.1 Numerical predictions of air-rush noise

Flow-induced noise issues in the car industry have traditionally been prevented by the use of empirical relations or engineering "know-how" in the early phases of car development programs. The outcome is typically followed up by measurements in mules, prototypes or production vehicles. These physical models are produced comparably late in the car programs as compared to the release of virtual geometry, which often means that problems detected at this stage must be solved in an ad hoc manner and sometimes with expensive solutions as a consequence. There is thus a need to develop methods that can be used early in car programs for taking control of and reducing the level of flow-induced noise. Virtual methods are well suited for this purpose.

Numerical attempts to solve George's [5] four steps have been made in the last decade. The two dominant techniques for predicting automotive separation dynamics as a starting point for wind noise predictions are the traditional Finite Volume Method (FVM) and the Lattice Boltzmann Method (LBM).

One of the first attempts covering the first two steps in George's list for a sedan is the work of Ono et al. [10], published in 1999. They conducted unsteady incompressible flow simulations to find the surface pressure fluctuations by means of a third-order upwind biased scheme for the convective terms instead of modeling the sub-grid stresses commonly used in the LES spatial filtering approach. The size of their simulation covered approximately 2.6 million grid points. Measured and simulated pressure fluctuation levels showed good agreement at the investigated points located at the vehicle surface. They also presented an interesting approach to reduce the wind noise based on the use of a combination of simulations and measurements. They used the predicted results to find separation zones and regions with high pressure fluctuations. This information was then used to modify the mirror and A pillar geometry to reduce the noise emitted to the compartment. With this approach they typically managed to reduce the overall noise levels by about 2 [dB].

In 2002, Rung et al. [11] conducted a flow and noise radiation study of a generic side mirror in comparisons of Unsteady Reynolds Averaged Navier-Stokes (URANS) and Detached Eddy Simulations (DES). They compared surface pressure fluctuations and radiated sound computed by the Ffowcs-Williams and Hawking's equation [12] with corresponding measured results. They covered in other words the three first steps in George's list. Their findings showed a major improvement in the predicted acoustic sources and the radiated sound using the DES model for most surface-mounted sensors and microphones as compared with the URANS results.

Posson and Pérot [13] took the geometry complexity one step further by mounting a production mirror on top of a plate and exposing it to a freestream velocity of 40 [m/s]. The flow field was solved by an incompressible LES approach with a tetrahedral dominant grid and 5-7 prism layers near the solid boundaries. The maximum number of cells in their work was about six million. The emitted sound was then computed using Ffowcs-Williams and Hawking's equation by evaluating both dipole and quadrupole sources. In the case with the finest resolution both mean and fluctuating velocity components were compared with PIV measurements, showing well predicted trends in all the evaluated regions.

Several authors [14–16] have also described the use of the LBM approach to estimate aero-acoustic noise sources in flow separated regions. Duncan et al. [14] made a simulation past the Ahmed body and used signal processing to visually identify noise sources restricted to different frequency bands.

Senthooran et al. [15] conducted a zero degree and a ten degree yaw angle simulation to validate simulated surface pressure spectra over the front side window as compared to measurements for a sedan type vehicle. The probes closest to the beltline and B pillar showed promising agreement up to about 1000 [Hz] when compared to the measurements for both yaw angles evaluated.

Gaylard [16] used a similar approach for a full vehicle including side mirrors and rails at a zero degree yaw angle. His results showed fair predictions of the surface pressure for some of the probes over the side window but, at most, an almost 40 [dB] offset at another location.

Finding the surface pressure fluctuations numerically requires an unsteady approach. One of the most promising techniques for solving complex turbulent flow problems is Large Eddy Simulations (LES), mainly due to the limitation of the Reynolds-Averaged Navier-Stokes (RANS) approach. Traditionally, LES has been considered too computationally expensive for industrial use because of its restriction to low and moderate Reynolds number flows. Computational capacity has gone through a tremendous evolution during the past decade, on the other hand, and flow simulations that were beyond the imagination only a few years ago are now regularly used in car programs to evaluate thermo and aerodynamic properties. One of the chief arguments for why unsteady flow simulations are too expensive for industrial use concerns the near-wall resolution in high Reynolds number flows, which is addressed in the next section.

2.2 Wall modeling techniques for high Reynolds number flows

In recent years wall resolved LES has gained increased attention as a result of several successful applications. The key to this success has been moderate Reynolds numbers or flows with homogeneity in one spatial direction. For high Reynolds number flows past three-dimensional objects, wall-resolved

LES is still out of reach for most engineering applications. The primary cause of this limitation is the need to resolve the streaks typically present in the near-wall region. Many estimations of the number of grid points required to resolve these kinds of flow structures are found in the literature [11, 17–20]. Chapman [17] estimated the grid requirement for resolving the boundary layer as

$$N_{xyz} \propto Re_L^{1.8} \tag{2.5}$$

for nested grids and flat plate boundary layers. This estimate is not far from the resolution requirements in DNS, where $N_{xyz} \propto Re_L^{9/4}$. Furthermore, Temmerman et al. [18] mention a grid dependency remote from walls as $N_{xyz} \propto Re^{0.4}$ in the outer region. This means that the outer region will typically contain only a fraction of the total number of grid points. In a more local perspective, these estimates can be expressed in terms of wall units for the first off-wall cells. In the wall normal direction, the resolution in wall units is similar to the requirement for a low Reynolds model, with $n^+ \approx 1$. The limitation in a wall-resolved LES compared to RANS occurs in the streamwise (s^+) and spanwise (l^+) direction of the flow. Spalart [19] recommended for wall-resolved LES that $s^+ \approx 50$; the corresponding recommendation in Davidson and Dahlström [21] was $s^+ \approx 100$. Davidson and Dahlström recommended $l^+ \approx 20$ in the spanwise direction, and similar values were presented in Temmerman et al. [18]. To circumvent this bottleneck in computational requirements for wall-resolved LES, a wide range of techniques have been developed to reduce the computational effort necessary in the near-wall region. A schematic overview of the different methods is presented in Fig. 2.1.

One way to circumvent the near-wall resolution issues in LES is by using wall functions. These functions replace the resolution requirement of the governing equations with an expression or value for the wall shear stress. Typical for these techniques is that the first off-wall cells are located in the logarithmic region of $30 < n^+ < 300$ where the lower limit is most desirable. In their simplest form, the log-law based wall functions assume logarithmic or semi-logarithmic velocity profiles that provide the wall shear stress as a boundary condition to the governing filtered or averaged equations. The drawbacks in this assumption are well known for flows involving separation, stagnation and reattachment, where the wall shear stress vanishes. To increase the validity of the wall functions, improvements have been made to include the pressure gradient, Wilcox [22], and to replace the wall shear stress in the velocity log-law with the turbulent kinetic energy, Craft et al. [23]. However, these treatments still rely on an assumed logarithmic or semi-logarithmic velocity

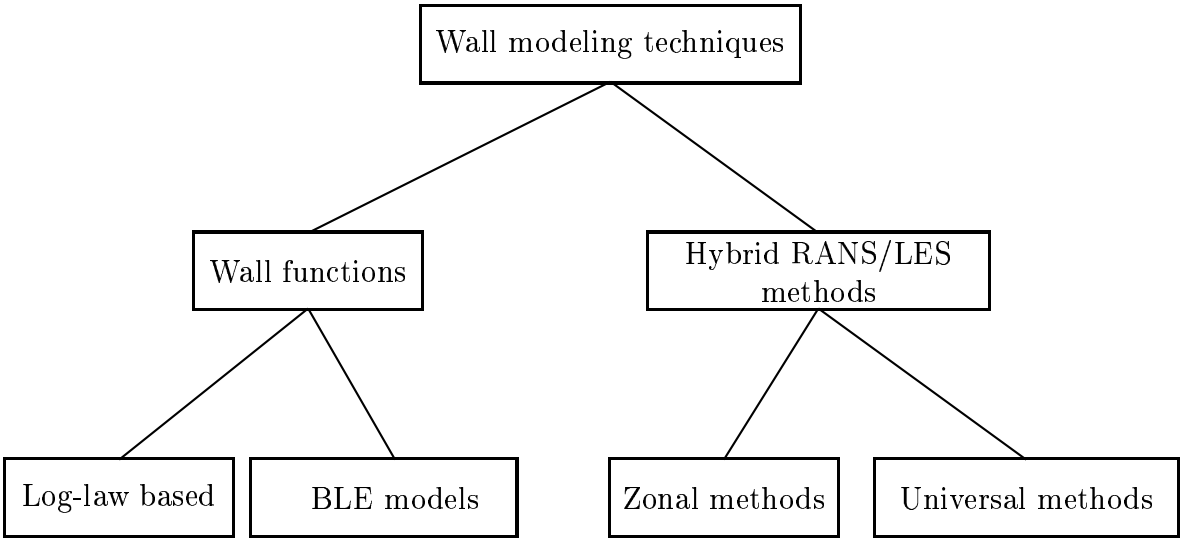

Figure 2.1: Overview of techniques for wall-bounded high Reynolds number flows, Boundary Layer Equations (BLE)

distribution, which drastically limits their validity.

Balaras and Benocci [24] described a different approach to wall modeling that was based on filtered Navier-Stokes equations and used what appeared to be a high Reynolds grid. The filtered equations were solved down to the first grid point on this primary high Reynolds grid. A refined mesh was embedded in the main mesh from the first grid point and down to the wall, where simpler two-dimensional Boundary Layer Equations (BLE) were solved. The boundary layer equations give velocity profiles for the streamwise and spanwise components and thus provide the wall shear stress in order to be able to solve the outer filtered equations. The advantages of this technique are twofold. First, less empiricism is needed to compute the wall shear stress compared to the logarithmic based wall functions mentioned above. Secondly and most attractive is that the cumbersome procedure of building low Reynolds meshes is avoided. This is a major advantage in industrial applications, where low Reynolds grids may prove almost impossible to generate due to the geometrical complexity. This technique was used in Cabot and Moin [25] for a backward facing step and was compared with wall resolved LES; it showed promising results for both wall friction and wall pressure. However, as pointed out in Nicoud et al. [20], a strong dependency on local Reynolds number and the location of the first off-wall cell are vital for an accurate prediction of the velocity profiles, which can be problematic in separated flows.

The technique was further investigated In Wang and Moin [26] for the airfoil trailing edge flow. The results showed a clear overprediction of the mean friction coefficient, which was argued to be caused by too high a turbulent viscosity. They suggested that a dynamically adjusted mixing-length eddy viscosity should be used instead to circumvent this problem. The resolutions in wall units for their simulation were ($s^+ \approx 60$) and ($l^+ \approx 30$), where the first off-wall node in the wall normal direction was located in the lower part of the logarithmic layer.

A different approach to solving the wall modeling issues is the hybrid RANS/LES techniques. Instead of using a refined sub-grid model, the steep wall normal gradients are resolved by the grid, i.e. by using a low Reynolds grid. Unlike wall-resolved LES the directions parallel to the wall will not be resolved. Thus, the near-wall structures are not resolved and the SGS model must be modified in this region to account for these unresolved motions. A possibility is to augment the SGS model with an ordinary RANS eddy viscosity model in the wall region. The fundamental idea is that the governing RANS equations are very similar to the LES equations except for the definition of the turbulent viscosity, as pointed out by Davidson and Dahlström [21]. The turbulent viscosity is proportional to a characteristic turbulent length and velocity scale, which is defined in different ways for RANS and LES. This type of technique can further be divided into two different categories based on the interface condition. Zonal methods refer to methods in which the interface is defined in advance and often in terms of wall units, while universal models have the inherent ability to switch between the two domains. For these techniques the crucial point seems to be how to transfer modeled turbulence from the RANS region to resolved stresses as boundary conditions to the LES domain. A direct consequence of the above described approach is that the near-wall solution will never be better than the embedded RANS model.

Two trends in the zonal techniques can be identified over the years. First, several studies aimed at embedding more physics in the RANS model and, second, investigations have been made of the RANS/LES interface position and the transition from RANS to LES. The studies have in their simplest form implemented one-equation models, Davidson and Dahlström [21] to two-equation models [27–29]. Efforts have recently been made to introduce true or synthetic fluctuations over the RANS/LES interface. The idea is to circumvent the poorly resolved stresses from the RANS region (Davidson and Dahlström [21]) and introduce either true turbulent fluctuations from a DNS over the interface or synthesized turbulent fluctuations, Davidson and

Billson [30]. An even more refined technique for improving the interface condition was evaluated in Nicoud et al. [20]. They used suboptimal control theory for the turbulent channel flow to force the outer LES solution toward a desired solution by using the wall stress boundary condition as a control. The drawback was that the computational cost for the channel flow was 20 times greater than for an explicit wall stress model.

In the final class of wall modeling techniques, "universal models", as proposed by Labourasse and Sagaut [31], will be discussed. Universal models are models that inherently switch between RANS and LES mode and apply the same equations in both regions. One of the most commonly used methods is the DES simulation technique used first by Spalart et al. [32]. In DES the same equations are solved for both the RANS and LES zones by using a simple one-equation model for the modified turbulent viscosity close to the wall. When the grid in all directions is much smaller than the boundary layer thickness, it smoothly turns into an SGS model. The essence of the model is the recognition of the DES length scale, $\widetilde{l}$, defined as

$$\widetilde{l} = \min(d_w, C_{DES}\Delta) \tag{2.6}$$

The DES length scale actually consists of the evaluation of two different length scales. The first RANS length scale, d_w, is based on the distance to the closest wall and the LES length scale, $C_{DES}\Delta$, depends on the grid spacing. The LES length scale is $\Delta = \max(\Delta x, \Delta y, \Delta z)$ and C_{DES} is the model constant, $C_{DES} = 0.65$, obtained from isotropic decaying turbulence. The two length scales will converge over the RANS/LES interface and contribute to a smooth transition between the zones. In contrast to the zonal models the approach has no issues concerning discontinuities in any variable over the zones. This is also one of its drawbacks because, in its basic form, it covers the whole boundary layer in the RANS mode. The method is intended for industrial applications at high Reynolds numbers, and promising results have been presented for several complex geometries and flow fields [11, 33–39].

A similar technique that circumvents grid dependency is the Scale Adaptive Simulation (SAS) model by Menter [40, 41]. The model uses, as compared to DES, a dynamic length scale based on locally resolved eddies in the flow. This length scale is defined as:

$$L_{vK} = \kappa \sqrt{\frac{\partial U_i}{\partial x_j}\frac{\partial U_i}{\partial x_j} \Big/ \frac{\partial^2 U_l}{\partial x_m^2}\frac{\partial^2 U_l}{\partial x_n^2}} \tag{2.7}$$

The method is still in its infancy and has so far only been evaluated for a minor number of flow fields. Both DES and the SAS model have however been evaluated for circular cylinders (Travin et al. and Menter et al. [34,40]) and have shown similar results in terms of the surface pressure distribution. Other techniques categorized together with the universal models include that presented by Speziale [42], who used a blending of the stress tensor in a Reynolds stress model, which makes it possible to transfer smoothly between RANS and LES. This idea was further developed in Batten el al. [43, 44] and was called the Limited Numerical Scale (LNS), where a parameter-free definition of the blending function based on products of turbulent length and velocity scales was used. In essence, the LNS approach identifies the resolved and unresolved fractions of the kinetic energy. The technique was also used for subdomain simulations involving RANS and LES and was then referred to as "embedded LES" through a forcing over the LES/RANS interface using synthetic turbulence, similar to the zonal methods described above.

It can be concluded from the discussion above that all the techniques named have drawbacks and advantages that can be more or less crucial for complex flows.

2.3 CAA Methodologies

A Direct Simulation (DS) is a flow simulation resolving all flow and acoustic scales without modeling and is an extension of Direct Numerical Simulations (DNS) primarily used for incompressible flow fields at low Reynolds numbers. The DS approach is therefore perhaps the most intuitive way to compute sound radiation since the equations of motion and energy combined with an equation of state fully describe both the flow and the acoustic field. With the DS approach it is therefore at least theoretically possible to directly evaluate sound emissions at any point in the computational domain, which is the one and perhaps only attractive attribute of the method. In DNS all flow scales are resolved, where the largest scale relates to the integral scale, L, and the smallest scale relates to the Kolmogorov microscale, η. The ratio between the largest and smallest scales depends on the Reynolds number of the flow according to

$$L/\eta \sim {Re_L}^{3/4} \tag{2.8}$$

where $Re_L = u_{rms}L/\nu$, see Tennekes and Lumley [45]. The relation (L/η) in each direction leads to a total spatial resolution being proportional to $(L/\eta)^3$,

or, in term of the Reynolds number as ${Re_L}^{9/4}$. Since the time step relates to the grid size through the CFL number, the computational effort then becomes proportional to $(L/\eta)^4$, or ${Re_L}^3$. In DS the largest scale is not necessarily the integral length scale L, but instead the distance, λ, between the source region and the observer. The ratio between largest and smallest scales then becomes (λ/η). The acoustic length scale is $\lambda = a/f$, where a is the speed of sound and f is the frequency; the corresponding turbulent relation is $L \sim u/f$. The computational effort for DS thus scales as $Ma^{-4}{Re_L}^3$, Sarkar and Hussaini [46]. Further, two physically different domains will exist, one near field or flow region which will be more or less incompressible for low Mach numbers with pressure fluctuations scaling as $\rho_\infty u^2$, and a far field or acoustic region where the pressure fluctuations will scale as $\rho_\infty a_\infty u$, where u is the particle velocity. The numerical schemes that should handle both regions are therefore very important. In addition, boundary conditions are needed that minimize sound wave reflections. Flows in automotive applications typically occur at both high Reynolds numbers and at low Mach number. DS will therefore be less relevant for solving these problems.

To circumvent the resolution bottleneck in DS the next step in an increased level of modeling concerns the assumption that the smallest flow scales are less efficient in generating sound than the larger scales. This assumption is justified for the compressible LES approach, where the smallest scales are separated from the largest scales by a filtering approach. This will significantly reduce the computational effort as compared to DS but the practical problems still remain. As for DS, the observer must still be located in the computational domain, which determines the size of the domain.

Another way to further decrease computational effort is to use wave propagation methods, such as the Kirchhoff-Helmholtz equation. These techniques make use of the existence of the two different regions. The hydrodynamic nonlinear region is typically resolved by compressible LES, and the pressure or density fluctuations are captured along an integral surface located outside the nonlinear region. This information is then used to propagate the pressure perturbations to an observer. One advantage is that the location of the observer is decoupled from the computational domain and can be chosen arbitrarily as long as it is located outside the integral surface. Another advantage of this technique as compared to DS is that numerical dissipation and dispersion in the propagation of sound waves over long distances are avoided, which may increase the accuracy of the results. The Kirchhoff-Helmholtz technique has successfully been used for jet applications; one example is the work by Andersson [47].

The third approach completely decouples the flow hydrodynamics from the acoustics and is the idea behind Lighthill's analogy and his successors Curle and Ffowcs-Williams and Hawkings. In principle, the acoustic analogies assume that the hydrodynamics of the flow is the main contributor to sound generation. The solution is then found by identyfing a medium at rest with pulsating sources that corresponds to the inhomogeneous part of a linear wave equation. These methods will be briefly described below.

2.4 The era of acoustic analogies

Lighthill's idea was to convert the governing compressible fluid equations to form a wave equation.

$$\frac{\partial \rho}{\partial t} + \frac{\partial \rho u_i}{\partial x_i} = 0 \tag{2.9}$$

$$\frac{\partial \rho u_i}{\partial t} + \frac{\partial \rho u_i u_j}{\partial x_j} = -\frac{\partial p}{\partial x_j} + \frac{\partial \tau_{ij}}{\partial x_j} \tag{2.10}$$

His starting point was the continuity equation, Eq. 2.9, and the momentum equations, Eq. 2.10, written in conservative form. In Eq. 2.10 the viscous stress tensor is defined as

$$\tau_{ij} = \mu \left(\frac{\partial u_i}{\partial x_j} + \frac{\partial u_j}{\partial x_i} - \frac{2}{3} \frac{\partial u_k}{\partial x_k} \delta_{ij} \right) \tag{2.11}$$

Subtracting the divergence of Eq. 2.10 from the time derivative of Eq. 2.9 gives

$$\frac{\partial^2 \rho}{\partial t^2} - \frac{\partial^2 \rho u_i u_j}{\partial x_i \partial x_j} = -\frac{\partial}{\partial x_i} \left(-\frac{\partial p}{\partial x_j} + \frac{\partial \tau_{ij}}{\partial x_j} \right) \tag{2.12}$$

Rearranging the terms in Eq. 2.12 gives

$$\frac{\partial^2 \rho}{\partial t^2} = \frac{\partial^2}{\partial x_i \partial x_j} \left(\rho u_i u_j + p \delta_{ij} - \tau_{ij} \right) \tag{2.13}$$

,where δ_{ij} is the Kronecker delta function.

$$a_\infty^2 \frac{\partial^2 \rho}{\partial x_i^2} - a_\infty^2 \frac{\partial^2 \rho \delta_{ij}}{\partial x_i \partial x_j} = 0 \tag{2.14}$$

If Eq. 2.14 then is subtracted from Eq. 2.12, the result will be an inhomogeneous wave equation with the wave operator on the left hand side and acoustic source terms on the right hand side: The result will then be Lighthill's equation:

$$\frac{\partial^2 \rho}{\partial t^2} - a_\infty^2 \frac{\partial^2 \rho}{\partial x_i^2} = \frac{\partial^2 T_{ij}}{\partial x_i \partial x_j} \tag{2.15}$$

In Eq. 2.15 the double divergence terms, T_{ij}, are commonly referred to as the Lighthill stress tensor, defined as $T_{ij} = \rho u_i u_j + (p - a_\infty^2 \rho)\delta_{ij} - \tau_{ij}$. Outside the turbulent region, Lighthill considered a medium governed by density ρ_∞, pressure p_∞ and speed of sound a_∞^2. In this region, the acoustic waves will be small perturbations about a state of rest according to $p = p_\infty + p'$ and $\rho = \rho_\infty + \rho'$, governed by the homogeneous wave equation $\frac{\partial^2 \rho'}{\partial t^2} - a_\infty^2 \frac{\partial^2 \rho'}{\partial x_i^2} = 0$. Lighthill's equation formulated in terms of density fluctuations can then be written as

$$\frac{\partial^2 \rho'}{\partial t^2} - a_\infty^2 \frac{\partial^2 \rho'}{\partial x_i^2} = \frac{\partial^2 T_{ij}}{\partial x_i \partial x_j} \tag{2.16}$$

,where T_{ij} is now $\rho u_i u_j + (p' - a_\infty^2 \rho')\delta_{ij} - \tau_{ij}$. In contrast, inside the turbulent or flow region, $\frac{\partial^2 \rho}{\partial t^2}$ will not be in balance with $a_\infty^2 \frac{\partial^2 \rho}{\partial x_i^2}$ but will instead result in an inhomogeneous wave equation with pulsating sources T_{ij}. Lighthill further discussed the magnitude of the three existing source terms in the T_{ij} tensor. Flows without entropy fluctuations will result in a balance between p' and $a_\infty^2 \rho'$, which was argued to be a fair assumption for cold jets. The viscous term τ_{ij} may also be neglected for high Reynolds number flows, which means that the only significant contribution to T_{ij} is the momentum flux tensor, $T_{ij} \approx \rho u_i u_j$.

Equation 2.15 is exact and, at least theoretically, valid everywhere as long as the flow field is known at every point and at every time. The solution to Lighthill's equation, Eq. 2.15, for an unbounded domain can be found through the use of a free-space Green's function, which is the retarded potential solution to the fundamental wave equation, see Morse and Feshbach [48].

$$\rho'(\mathbf{x}, t) = \frac{1}{4\pi a_\infty^2} \frac{\partial^2}{\partial x_i \partial x_j} \int_V \left[\frac{T_{ij}}{r}\right] d\mathbf{y} \tag{2.17}$$

The brackets in Eq. 2.17 mean that T_{ij} is to be evaluated at retarded time. If a decoupling between the acoustics and the flow can be made, then Eq. 2.17 is explicit, meaning that once the sources are found, the sound pressure

levels can be found without additional iterations. Secondly, the flow domain consists of a large variety of energy-containing structures or sources which by far exceeds the acoustic energy content. This is handled mathematically by solving Eq. 2.15 analytically, which serves as a filter that sorts important acoustic generating sources from the nonacoustic ones, which must otherwise be done numerically. A third aspect is that Lighthill's formulation also hints at an incompressible treatment of the flow, since, at low Mach number without temperature fluctuations, $\rho \approx \rho_\infty$, which gives that $T_{ij} \approx \rho_\infty u_i u_j$. A space-derivative form can also be obtained by the use of convolution products, which gives

$$\rho'(\mathbf{x},t) = \frac{1}{4\pi a_\infty^2} \int_V \left[\frac{1}{r} \frac{\partial^2 T_{ij}}{\partial y_i \partial y_j} \right] d\mathbf{y} \tag{2.18}$$

The two versions, Eq. 2.17 and Eq. 2.18, are mathematically identical but have different interpretations, discussed by Curle [49]. Equation 2.18 represents sound radiated by a distribution of quadrupoles with the strength T_{ij} in a medium at rest, while Eq. 2.17 considers the quadrupole field as four separate source fields infinitely close to each other.

Several approximate versions of Lighthill's integral formulation exist in addition to Eq. 2.17 and Eq. 2.18 for observers located in the farfield. These are:

$$\rho'(\mathbf{x},t) = \frac{1}{4\pi a_\infty^2 |\mathbf{x}|} \frac{\partial^2}{\partial x_i \partial x_j} \int_V [T_{ij}]\, d\mathbf{y} \tag{2.19}$$

$$\rho'(\mathbf{x},t) = \frac{1}{4\pi a_\infty^4 |\mathbf{x}|} \frac{x_i x_j}{|\mathbf{x}|^2} \int_V \left[\frac{\partial^2 T_{ij}}{\partial t^2} \right] d\mathbf{y} \tag{2.20}$$

$$\rho'(\mathbf{x},t) = \frac{1}{4\pi a_\infty^2 |\mathbf{x}|} \int_V \left[\frac{\partial^2 T_{ij}}{\partial y_i \partial y_j} \right] d\mathbf{y} \tag{2.21}$$

In Sarkar and Hussaini [46] formulations Eq. 2.20 and Eq. 2.21 were evaluated for isotropic turbulence and a single imposed quadrupole. One conclusion drawn from their work was that the spatial formulation, Eq. 2.21, required a time step size in the order of Ma^2 smaller than the temporal formulation, Eq. 2.20.

Lighthill also managed to find a relation between the simplified Lighthill tensor, $T_{ij} \approx \rho u_i u_j$, and the radiated power, scaling as an eight-power dependency on flow speed for low Mach number flows in the absence of boundaries. However, most practical flows are bounded by walls to different extents.

More generalized theories based on Lighthill's theory were thus later developed to include solid boundaries, Curle [49], as well as moving and permeable surfaces, Ffowcs Williams and Hawkings [12]. The derivation of Curle's equation involves two more steps than in Lighthill's equation. First, the presence of boundaries adds a surface integral to the volume integral through the Kirchhoff-Helmholtz formula. Secondly, Curle transformed Eq. 2.18 with the Kirchhoff-Helmholtz formula from source coordinates to observer coordinates, which induces additional surface terms. His final expression states

$$\rho'(\mathbf{x},t) = \frac{1}{4\pi a_\infty^2}\frac{\partial^2}{\partial x_i \partial x_j}\int_V \frac{1}{r}\left[T_{ij}\right] dV(\mathbf{y}) - \frac{1}{4\pi a_\infty^2}\frac{\partial}{\partial x_i}\int_S \frac{n_j}{r}\left[p\delta_{ij} - \tau_{ij}\right] dS(\mathbf{y}) \tag{2.22}$$

Similar to the Lighthill equation, Curle's equation can also be derived in temporal form based on the acoustic pressure fluctuations instead of density according to Eq. 2.23, which was investigated by Larsson [50].

$$\begin{aligned} &p'(\mathbf{x},t) = \\ &\frac{1}{4\pi}\int_V \left[\frac{l_i l_j}{a_\infty^2 r}\ddot{T}_{ij} + \frac{3l_i l_j - \delta_{ij}}{a_\infty r^2}\dot{T}_{ij} + \frac{3l_i l_j - \delta_{ij}}{r^3}T_{ij}\right] dV(\mathbf{y}) \\ &+\frac{1}{4\pi}\int_S l_i n_j \left[\frac{\dot{p}\delta_{ij} - \dot{\tau}_{ij}}{a_\infty r} + \frac{p\delta_{ij} - \tau_{ij}}{r^2}\right] dS(\mathbf{y}) \end{aligned} \tag{2.23}$$

Compared to Lighthill's farfield version Eq. 2.20, the volume integral now contains additional terms which traditionally are neglectected for observers located in the farfield. In Eq. 2.23 both these near and farfield terms are kept and represent the acoustic pressure fluctuations at an observer located at $\mathbf{x}$ at observer time t. The acoustic pressure is evaluated from a retarded time projection of two integrals evaluated at the source location, $\mathbf{y}$. The first integral contains the volume contribution, as in the Lighthill equation, Eq. 2.20. The dot(s) above T_{ij}, τ_{ij} and p denote time derivative(s), and l_j is the unit vector pointing from the source to the observer. The second integral contains the surface integral and consists mainly of the pressure and the pressure temporal derivative.

The major assumption made in both Lighthill and Curle's equation concerns the decoupling between the acoustics and the flow hydrodynamics. The density or pressure fluctuation, which is the dependent variable, exists on both sides of the equation and, when explicitly solving the acoustics based on the source field, the acoustics will be decoupled from the source field. This is a

reasonable assumption for low Mach number flows but excludes fluid-resonant phenomena.

By increasing the generalization of Lighthill's equation, reflection and diffraction of the quadrupoles due to solid boundaries as well as dipole-generated noise were included in the source description, Curle [49]. In a similar manner as Lighthill, he managed to show that the additional dipole distribution caused by the solid boundaries gave a radiated power scaling as a six-power dependency on flow speed for low Mach number flows.

The effect on the aeroacoustic scaling laws of the increased generalization of the theory was also further discussed by Crighton [51], who studied the effect on the scaling laws for monopoles, dipoles and qudrupoles for both low and high Mach number flows. These scaling laws, revised in Appendix A, show that the functional laws for monopoles, dipoles and quadrupoles from a driver's perspective and low Mach numbers are also valid for ground vehicles. They are summarized in Eqs. 2.24 to 2.26.

$$p'_m(x) \propto u_m^2 \frac{l_m}{|\mathbf{x}|} \tag{2.24}$$

$$p'_d(x) \propto u_d^2 \frac{l_d}{|\mathbf{x}|} Ma_d \tag{2.25}$$

$$p'_q(x) \propto u_q^2 \frac{l_q}{|\mathbf{x}|} Ma_q^2 \tag{2.26}$$

We return to one of the main objectives of choosing a method with the capability to predict air-rush noise inside a ground vehicle. These flows occur at low Mach numbers, approximately 0.1. This hints at a monopole and dipole dominant sound field inside the compartment, which was supported by the findings of Watanabe et al. [8]. Possible choices are therefore Curle's and Ffowcs-Williams and Hawking's equation. The proposed method aims at determining the location and level of the most dominant sources, i.e the noise generation, mainly because of the problems involved in covering the whole chain from acoustic sources to transmission through the vehicle structure and in the end to determine the compartment noise. Until this is solved, a formulation should be chosen where the sources appear explicitly since the external noise radiation is not the main concern. Both the temporal formulations, Eq. 2.20 and Eq. 2.21 fulfill this requirement and both were investigated by Sarkar and Hussaini [46]. They found Eq. 2.20 to be far less computationally demanding than the spatial formulation Eq. 2.21. Further,

the temporal formulation of Curle, Eq. 2.23, showed promising results for the open cavity case, where the sources similarly appear explicitly. On the basis of these findings and criteria posed the temporal formulation of Curle is used for evaluation in this thesis.

2.5 Importance of compressibility

Flows around ground vehicles are typically low Mach number flows owing to the speed restriction on most roads. At a speed of 140 [km/h] the ambient Mach number will correspond to about 0.1, and an estimate of the errors made in assuming the density constant is then in the order of Ma^2, see Appendix B. This is why low Mach number flows are approximated with incompressible methods. On the other hand, sound is a strictly compressible phenomenon even if the Mach number is close to zero, which is the case for many underwater applications. In a compressible flow, the sources, or right hand side of Lighthill's or Curle's equation, will at a given instant in time contain both effects of turbulence and acoustic waves. In an incompressible flow, the latter contribution will be lost and the sources will thus only describe acoustics caused by hydrodynamics. Since the energy content of the hydrodynamics will be several orders larger than the acoustic part at low Mach numbers, the assumption may seem appropriate, at least for unbounded flows. However, for wall-bounded flows, for example in the HVAC or the exhaust system, a significant part of the acoustic energy may be caused by reflections, which will then be lost.

Solving the acoustics in low Mach number flows by means of an explicit compressible code is a significantly more CPU intensive activity than computing the flow field by an incompressible approach. This is primarily due to the vast differences in time scales for the acoustics as compared to the hydrodynamics. Lighthill's main interest was low Mach number cold jet flows where entropy fluctuation could be neglected. He identified the primary source of the noise radiation in the absence of walls as the momentum flux tensor. This directly hints at an approach where the sources are computed in an incompressible manner. However, if Lighthill's or Curle's equation are to be derived from the governing incompressible equations directly, the left hand side will be identical to zero. The approach is then to derive the scalar wave equation from the governing compressible equations and to make the assumption that $T_{ij} \approx \rho u_i u_j$ still when the fluid is considered compressible, and as a last step

to realize that the advection is essentially the same, whether computed as compressible or incompressible.

Chapter 3

Characterization of air-rush noise

Since this thesis is restricted to wall-bounded, low Mach number flows, the question is addressed of the degree to which the functional or scaling laws, Eq. 2.24 to Eq. 2.26, match the levels measured inside a production vehicle when air-rush noise is the main concern.

Handling all terms in for example Curle's equation requires evaluation of 22 terms: 18 volume terms and four surface terms. This means that isolating the most dominant source terms can significantly reduce the computational effort. To check whether this is acceptable for ground vehicles, a validation study was conducted to compare measured sound pressure levels in an existing production vehicle with the three source types presented in Eqs. 2.24 to 2.26. The measurement was made in Ford's acoustic wind tunnel in Merkenich. A microphone was placed at the driver's left ear position during a velocity sweep ranging from 10 [m/s] up to a maximum speed of 50 [m/s].

Calibration constants β and λ were introduced to match the curves at mid-speed, $U = 30$ [m/s]. The sound pressure levels were then computed according to

$$SPL(dB)_{Monopoles} = 20log_{10}\left(\frac{\frac{\rho}{4\pi|\mathbf{x}|}(\beta_m U_\infty)^2\lambda_m}{2\cdot 10^{-5}}\right) \tag{3.1}$$

$$SPL(dB)_{Dipoles} = 20log_{10}\left(\frac{\frac{\rho}{4\pi a_\infty |\mathbf{x}|}(\beta_d U_\infty)^3 \lambda_d}{2 \cdot 10^{-5}}\right) \quad (3.2)$$

$$SPL(dB)_{Quadrupoles} = 20log_{10}\left(\frac{\frac{\rho}{4\pi a_\infty^2 |\mathbf{x}|}(\beta_q U_\infty)^4 \lambda_q}{2 \cdot 10^{-5}}\right) \quad (3.3)$$

The physical interpretations of Eqs. 3.1 to 3.3 are as follows:

A monopole dominant sound character would imply insufficient seal design, causing leakages between the exterior and the compartment. These leakages would give rise to mass flow fluctuations at local spots typically along the splitlines at the left mirror sail, mirror head, front side window or door, which may then dominate over the other sources due to their relatively short distance to the driver's left ear position.

A dipole dominant sound character could have two implications. First, separated flow regions will give rise to pressure fluctuations over the vehicle exterior that might transmit through the windows and seals. Secondly, steady leakage flows may also cause sources of a dipole character since mass flow injections would behave very much the same as small scale jets, which may cause pressure fluctuations at the walls of the compartment.

A quadrupole dominant sound character would imply that the turbulence in the free shear layers, for example downstream of the side mirror and A pillar, causes the noise, which transmits through the side windows in a similar manner as the surface pressure fluctuations. In the case of the dipoles, steady leakage flows can also give rise to quadrupole sources since an eventual leakage flow may contain turbulence in its shear layers.

The overall sound pressure level as a function of the freestream velocity is presented in Fig. 3.1, where the grid spacing along the y axis corresponds to a 10 [dB] increment, since the absolute values are company confidential. It is clear in Fig. 3.1 that the compartment sound pressure level scales with dipoles, indicating that surface pressure fluctuations are the dominating sources of the compartment noise levels. The overall sound pressure level is however a rather rough tool for investigating these effect since the frequency dependency is lost. The frequency range where air rush noise is most dominant is between 500 [Hz] and 5000 [Hz]. For this purpose the sound pressure level is also shown at four discrete frequencies, Fig. 3.2(a) to Fig. 3.2(d). The result of these figures also supports there being no significant frequency dependency, at least for the four frequencies investigated.

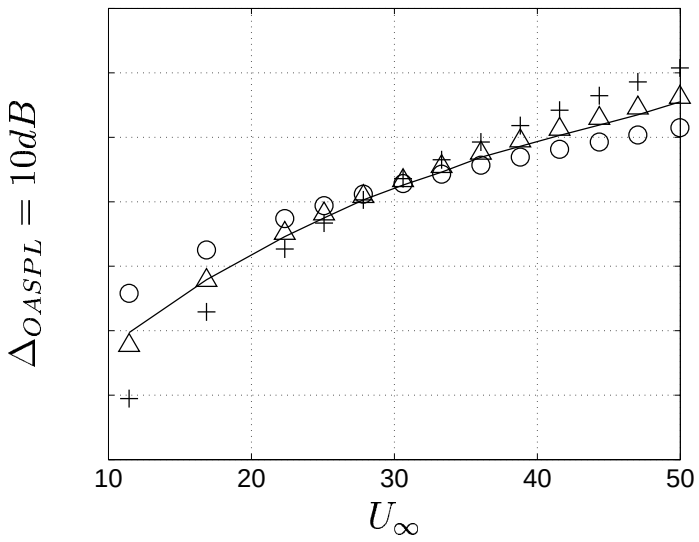

Figure 3.1: OASPL as a function of freestream velocity for a production vehicle, Measured (−), Qadrupoles (+), Dipoles (△), Monopoles (∘)

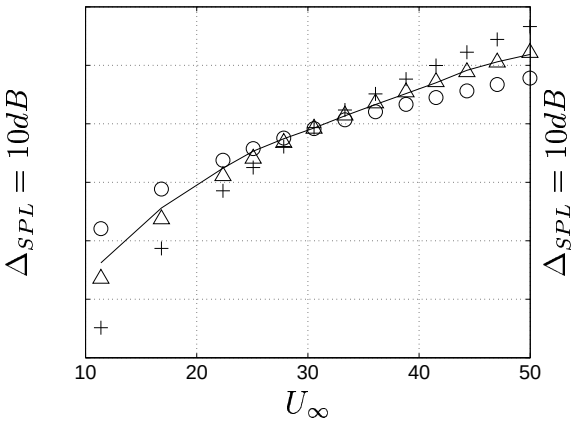

(a) SPL as a function of freestream velocity, $f = 500(Hz)$

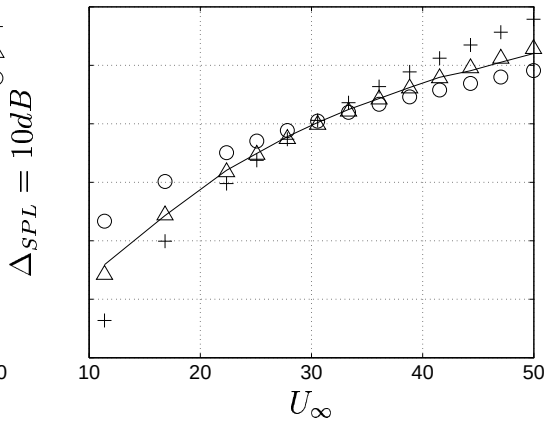

(b) SPL as a function of freestream velocity, $f = 1000(Hz)$

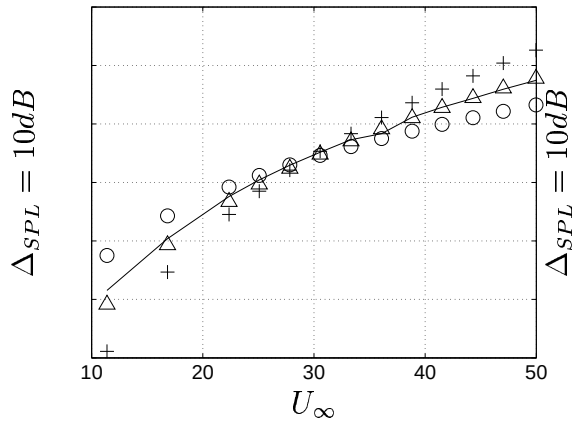

(c) SPL as a function of freestream velocity, $f = 2000(Hz)$

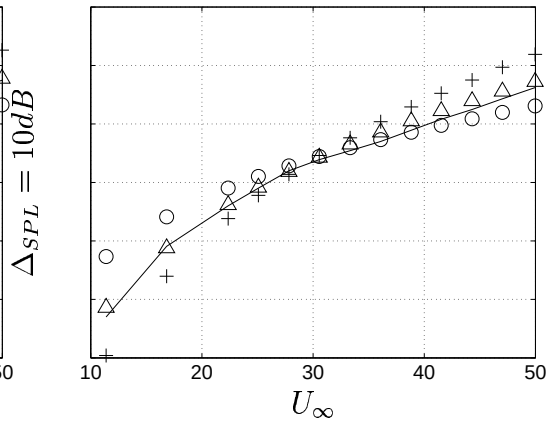

(d) SPL as a function of freestream velocity, $f = 4000(Hz)$

Figure 3.2: Multipole scaling laws applied to a production vehicle, Measured ($-$), Qadrupoles ($+$), Dipoles ($\triangle$), Monopoles ($\circ$)

Chapter 4

Buffer zone evaluation

Convection of strong vortices through the computational domain can cause numerical problems when they pass the outlet. These vortices can cause local backflow with erroneous results as a consequence. The wake mode flow regime of the open cavity investigated in this thesis is such a case. The remedy in these occasions is traditionally to extend the domain far downstream, to increase the grid stretching or to change the outlet boundary condition.

Here, an alternative solution to this problem is investigated by adding dissipative source terms to the governing equations, which are commonly referred to as *buffer zones*, *fringe zones* or *sponge zones* in the literature. This technique is predominantly used in direct simulations to prevent sound wave reflections generated by the outlet from polluting the sound field in the interior domain. The advantage in compressible simulations is that both the flow field and the sound waves can be damped over the buffer zone when propagating toward the outlet. In addition, pressure perturbations caused by the outlet boundary condition can be damped when they are reflected back into the domain through the buffer zone.

In incompressible simulations, no sound waves are present and distortions in the pressure will spread instantaneously in the whole domain and may contaminate the acoustic source terms. The purpose of buffer zones in this context is instead to dissipate the vorticity by forcing the velocities to reach a defined target level.

The test case used for the buffer zone evaluation is a convected vortex com-

puted in two dimensions. This test case serves mainly as a prestudy for the open cavity case. Both geometrical dimensions and physical properties are thus chosen to be as similar as possible. The Reynolds number of $Re = 1500$ is based on the freestream velocity, $U_\infty = 1.0$, the density, $\rho = 1.0$, and a unit length which for now is denoted D.

The computational domain is bounded by an inlet at $x_1 = -4.3D$, and the buffer zone entrance plane or resolved domain outlet is located at $x_1 = 14.0D$. The upper boundary is placed at $x_2 = 11.0D$, and the lower boundary is positioned at $x_2 = 0$. A visual representation of the domain is shown in Fig. 4.1, together with the coordinate system.

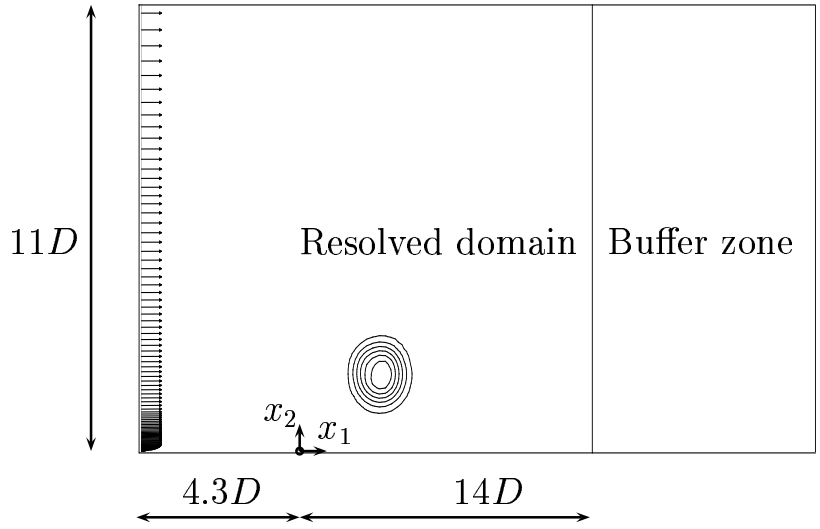

Figure 4.1: Test case description

The initial field consists of a disturbance superimposed to a laminar boundary layer profile, where the initial disturbance is defined as

$$v_t(x_1, x_2) = -\beta r^2 \exp[-\alpha r^2] \tag{4.1}$$

In Eq. 4.1, $r = \sqrt{(x_1 - x_{1,init})^2 + (x_2 - x_{2,init})^2}$, $\beta = 6$ and $\alpha = 2$. Its initial position is $x_{1,init} = 2.3D$, $x_{2,init} = 1.7D$ and the laminar velocity profile applied at the inlet is shown in Fig. 4.2. Other boundary conditions used in the test case are a no slip condition at the lower boundary and a symmetry condition at the upper boundary. The buffer zone is the region where the

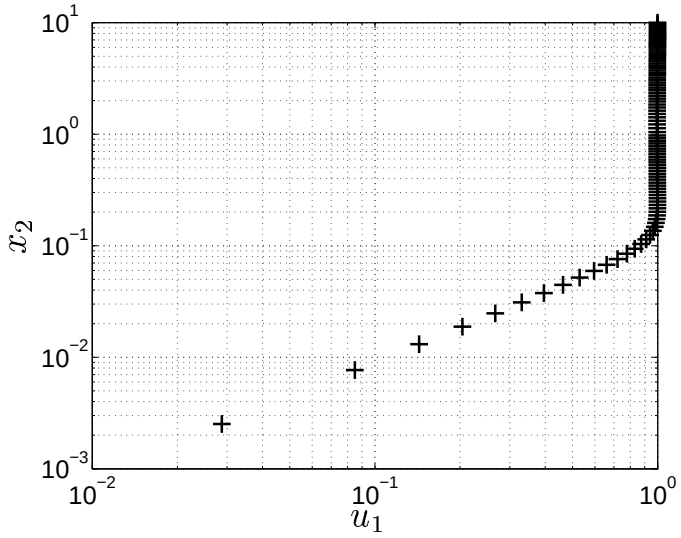

Figure 4.2: Mirror and plate, $x - z$ plane

damping source terms are active. Here, they are defined as

$$\rho \left(\frac{x_1 - x_{1,min}}{x_{1,max} - x_{1,min}} \right)^n \sigma \frac{U_\infty}{L} \left(u_i - u_i^{target} \right) \tag{4.2}$$

where n is a shape parameter. The amplification parameter, $\sigma \frac{U_\infty}{L}$, is in this case chosen to be 1.0 $[s^{-1}]$, and u_i^{target} is the target state, here defined as the local time-averaged velocity vector. The source term, Eq. 4.2, is further divided into a constant and a linear part and added to the momentum equations. The code used for the buffer zone study is the structured Finite Volume Method code, CALC-BFC, documented in Davidson and Farhanieh [52].

The main objective of the present study is to find a generic relation between the strength of the vortex and the buffer zone characteristics for a mean vortex convection speed. For this purpose, the vorticity is monitored over the buffer zone entrance plane. The vorticity in two dimensions is computed as

$$\Omega_z = \frac{\partial u_2}{\partial x_1} - \frac{\partial u_1}{\partial x_2} \tag{4.3}$$

Furthermore, this vorticity is averaged in the x_2 direction and monitored over time, which results in the integral value, I_ω, defined as

$$I_\omega = \frac{\int_0^H (\Omega_z^{rms}) dx_2}{H} \tag{4.4}$$

where $H = 11D$. The cases investigated for the buffer zone study are pre-

Buffer zone parameter study			
Case	NC/XB	Discretization scheme	n
CBC	0	C	-
CBV	0	VL	-
B1	20/3.657	CDS	2
B2	20/3.657	VL	2
B3	40/7.310	CDS	2
B4	40/7.310	VL	2
B5	40/7.310	CDS	1
B6	40/7.310	VL	1

Table 4.1: Buffer parameters and discretization schemes

sented in Table 4.1, where NC and XB are the number of cells in the x_1 direction and the length of the buffer zone, respectively. The two advection schemes used in the present study are the Van Leer scheme (VL) and a second-order central scheme (CDS). The shape parameter, n, corresponds to the exponent used in Eq. 4.2. The two cases, CBC and CBV, serve as reference solutions in which a convective outlet boundary condition is used, located at $x_1 = 14D$. The time step size used for the test case is $\Delta t = 0.05$, which corresponds to a maximum convective CFL number of $CFL_{max} \approx 0.3$. The wall pressure fluctuation level is computed as

$$SPL = 20log_{10}\frac{p_w^{rms}}{p_{ref}} \tag{4.5}$$

where $p_{ref} = \sqrt{\rho_\infty a_\infty 10^{-12}}$ and p_w is the surface pressure.

Results of the different cases are presented in Figs. 4.3(a) to 4.3(d). Figures 4.3(a) and 4.3(b) show the RMS values of the pressure along the lower wall extending from the inlet to the buffer zone entrance plane. When the convective boundary condition is used, increased pressure fluctuations are found over those found in the buffer zone cases, Figs. 4.3(a) and 4.3(b). The cause of the results in these two figures can be understood by looking at the time sequence of the pressure at a point located at $x_1 = 4.2D$ and $x_2 = 0$, Figs. 4.3(c) and 4.3(d). When the convective boundary condition is used, both advection schemes return a pressure disturbance when the vortex leaves the domain, although its amplitude is significantly higher for the CDS scheme than the

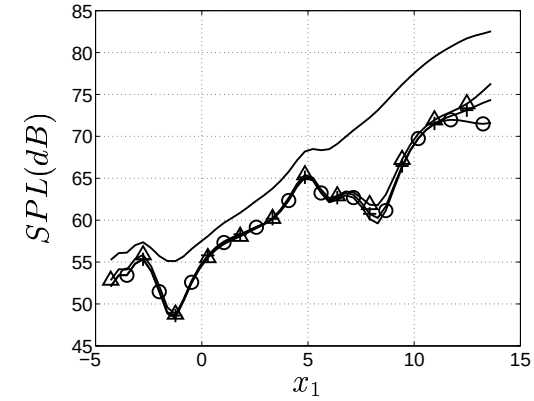

(a) Wall pressure levels for the central schemed cases CBC (−), B1 (△), B3 (∘), B5 (+)

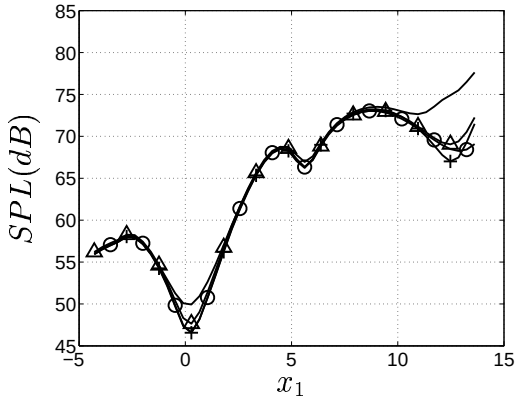

(b) Wall pressure levels for the upwind schemed cases CBV (−), B2 (△), B4 (∘), B6 (+)

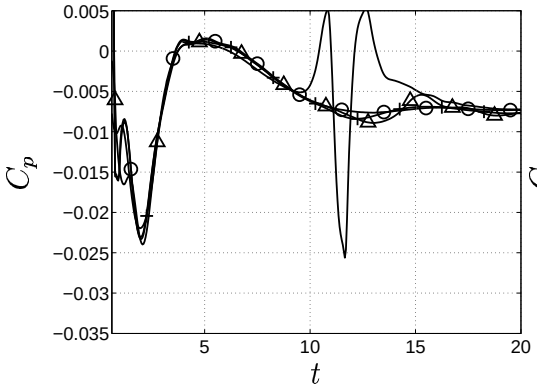

(c) Time series of C_p at $x_1 = 4.2D$, $x_2 = 0$ for the central schemed cases CBC (−), B1 (△), B3 (∘), B5 (+)

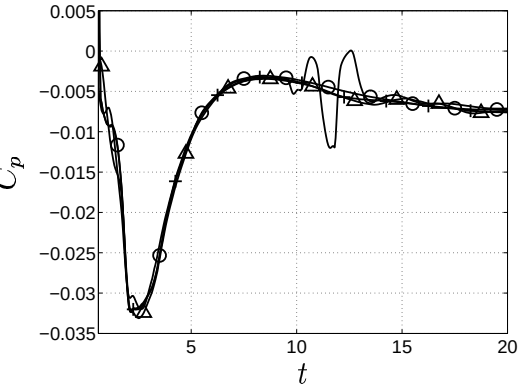

(d) Time series of C_p at $x_1 = 4.2D$, $x_2 = 0$ for the upwind schemed cases CBV (−), B2 (△), B4 (∘), B6 (+)

Figure 4.3: Results of the buffer zone evaluation according to Table 4.1

Van Leer scheme. This problem can partly be avoided by using a buffer zone, even though a small disturbance can be found in the range of $11 < t < 17$ for the CDS cases. The lowest distortion in C_p for the CDS cases is found for case B3, Fig. 4.3(c).

Regarding the vortex strength, all cases return similar results, Table 4.2, and tend to be slightly more sensitive to the advection scheme chosen as compared to the buffer zone length and shape, Fig. 4.3. The most critical cases are the

Buffer zone results	
Case	I_ω
CBC	-
CBV	-
B1	0.167
B2	0.145
B3	0.163
B4	0.142
B5	0.167
B6	0.144

Table 4.2: Vortex strength results for the different cases

central schemed cases, with a maximum vortex strength of $I_\omega \approx 0.167$, as compared to $I_\omega \approx 0.145$ for the upwind biased cases.

For the open cavity case (see Paper II), a linear relation between the vortex strength at the entrance plane of the buffer zone and the required length of the buffer zone is assumed, i.e.

$$L^{OC} = L^{B3}\frac{I_\omega^{OC}}{I_\omega^{B3}} \tag{4.6}$$

In Eq. 4.6, superscripts B3 are the values found in case B3, and OC corresponds to the open cavity case without a buffer zone. Case B3 is chosen because this case showed the lowest pressure distortions at location $x_1 = 4.2D$, $x_2 = 0$, Fig. 4.3(c), combined with strong vorticity at the buffer zone entrance plane. From this assumption, a minimum required length of the open cavity buffer zone can be estimated on the basis of the findings in case B3 and the vortex strength computed for the open cavity cases. This assumption requires that the vortex convection speed is approximately the same and that a linear assumption between different cases can be made.

Chapter 5

Open cavity reference case

All incompressible open cavity simulations conducted in this thesis are compared against a direct simulation made by Larsson [50]. Due to their central part in the open cavity investigation, some information on methodology and case set-up is repeated here to give an overview of the present state of the different simulations. The reference case is entirely the work of Larsson [50,53], and the interested reader is referred to these two publications. The computational domain in this reference case is defined in Fig. 5.1. The advection scheme used for the inviscid fluxes was the fourth-order accurate Dispersion Relation Preserving (DRP) scheme of Tam and Webb [54]. In time an explicit four-stage, fourth-order accurate Runge-Kutta algorithm was used. The spatial resolution in the reference case was approximately 80 cells per unit length in and in the vicinity of the cavity. Outside the cavity, the grid was stretched less than 1%. The time step increment was kept to $\Delta t = 0.001$. The boundary conditions in any flow simulation are of greatest importance, especially when analyzing acoustics. The boundary conditions used in the reference simulation are based on characteristic variables that are only non-reflective for orthogonal impinging waves. To prevent eventual reflections, both the inlet, outlet and farfield region were provided with buffer zones modifying the governing equations as follows:

$$\frac{\partial Q}{\partial t} + \frac{\partial E_j}{\partial x_j} = \frac{\partial F_j}{\partial x_j} - \sigma \xi^2 \left(Q - Q^* \right) \tag{5.1}$$

where Q is the state vector, E_j represents the inviscid fluxes, F_j represents the viscous fluxes and the time averaged target state is Q^*. The buffer parameter ξ, is the nondimensional distance from the buffer zone entrance

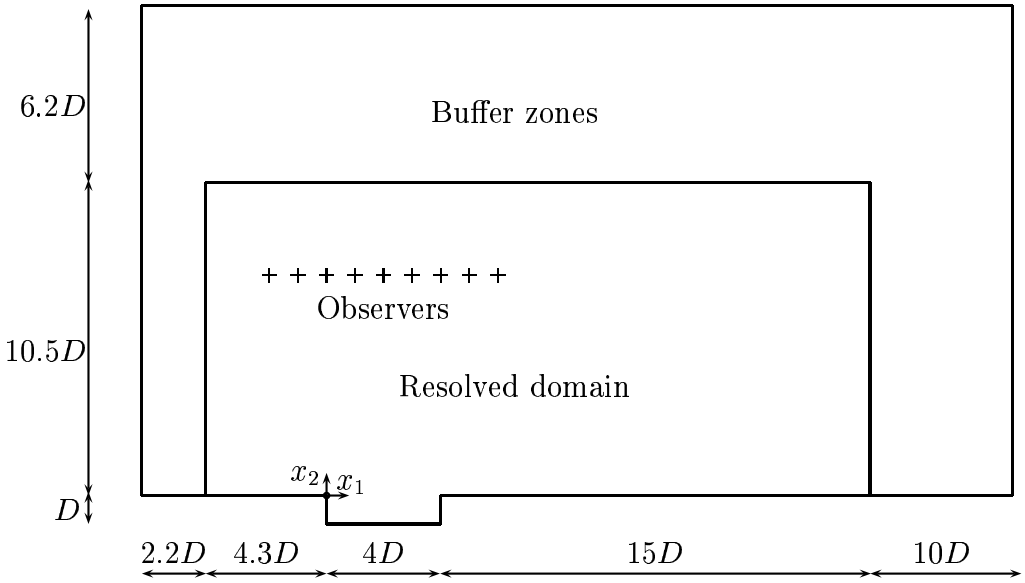

Figure 5.1: Computational domain, Reference case

plane to the outlet defined as, (x/L_b), where x is the distance from the start of the buffer zone and L_b is the length of the buffer zone. The damping parameter is $\sigma = \sigma_0 a/L_b$, where a is the speed of sound. The values of the nondimensional amplification parameter, σ_0, are: $\sigma_0 = 11.7$ at the inlet, $\sigma_0 = 2.07$ at the outlet and $\sigma_0 = 11.2$ in the farfield region.

The shortest wave length of interest was computed from the streamwise force coefficient spectrum, where most of the energy was contained below a Strouhal number of $St \leq 4$ based on the cavity length. The minimum wave length was then computed as follows:

$$\lambda_{min} = \frac{a_\infty}{f_{max}} = \frac{(U/Ma)}{(St_L \cdot U/L)} = \frac{L}{Ma \cdot St_L} \tag{5.2}$$

Inserting $L = 4$, $Ma = 0.15$ and the maximum Strouhal number, $St_L = 4$, gives the shortest wave length of interest, $\lambda_{min} \approx 7D$. In the vicinity of the cavity, the resolution is about 80 cells per cavity depth unit resulting in an approximate resolution of 500 cells for this wave length.

This brief summary gives relevant background information for the numerical approach and case definitions for the reference case.

Chapter 6

Complementary results

6.1 The open cavity

The different results in the overall sound pressure level reported in Paper I and Paper II for the incompressible cases are further discussed here to perhaps gain a better understanding of these different results. The basic argument for the conclusion of a phase mismatch between the compressible and incompressible solutions is that the level of the observer signature is caused either by the amplitude of the different source contributions or the phase of the different sources. The source fluctuation levels in Fig. 5 in Paper II showed an almost perfect match between the different cases in the vicinity of the cavity, which supports the conclusion that the level of the most energy-containing sources are correctly predicted even if treated as incompressible. The conclusion was therefore drawn that the main cause to a mismatch in sound pressure levels concerns phase shifts between sources predicted from different flow fields. This might be too hasty a conclusion since sound radiation is caused by cancellations or amplifications of different sources. This means that, even if the amplitude of the most dominant structures are captured correctly, which is what the RMS level represents, large deviations in the total acoustic pressure can still occur if small perturbations occur at a point in time when the main sources cancel each other. One way to analyze this situation is instead to study the acoustic signature from the different surface segments directly.

The cases in Paper II were as follows, Table 6.1.

Description of cases			
Case	Outlet treatment	End of resolved domain	End of domain
Ref	Buffer zone	19D	29D
C1	Buffer zone	14D	19D
C5	Convective bc	35D	35D

Table 6.1: Description of the cases according to Paper II

Of the nine observers, the largest discrepancy was found for observer seven, located directly above the cavity. Therefore this observer was used in the following analysis.

The effect on the acoustic signals of using the buffer zone as compared to the convective outlet boundary condition is shown in Fig. 6.1. The integration region used in this figure contains the walls extending from the inlet to $14D$ downstream of the cavity leading edge, and both source terms are used to obtain the acoustic signals.

For both cases, $C1$ and $C5$, the computational time step is $\Delta t = 0.005D/U_\infty$. The effect of the two major vortices leaving the domain is clearly seen in Fig. 6.1 as two peaks at time $tU_\infty/D \approx 38$ and $tU_\infty/D \approx 47.5$. With the use of the buffer zone, these disturbances are significantly reduced but seem to amplify the high frequency oscillations in the time span $35 < tU_\infty/D < 40$. This may be an effect of the buffer zone itself or possibly an effect still present in case C5 but masked due to the distorted pressure field caused by the outlet boundary condition. Since the largest discrepancy was found for observer seven, another possibility is that the oscillations could also be caused by the singularity at the cavity trailing edge which might create problems for an incompressible flow field. In addition to the high frequency oscillation existing in case C1, major discrepancies in the acoustic signals still exist over more or less the whole period. In the work reported in Paper II, it was found that a part of the error was related to the inlet boundary condition. This was circumvented by skipping the wall extending from the inlet to the cavity leading edge in the surface integration. It was also argued that a possible mismatch in phase could be the cause of the results shown in Fig. 10(a) and Fig. 10(c) in Paper II, when shifting the integration region from the cavity bottom wall to the remaining walls extending from the cavity leading edge to the outlet ($x_1 = 14D$). One way to study these possibilities is to plot

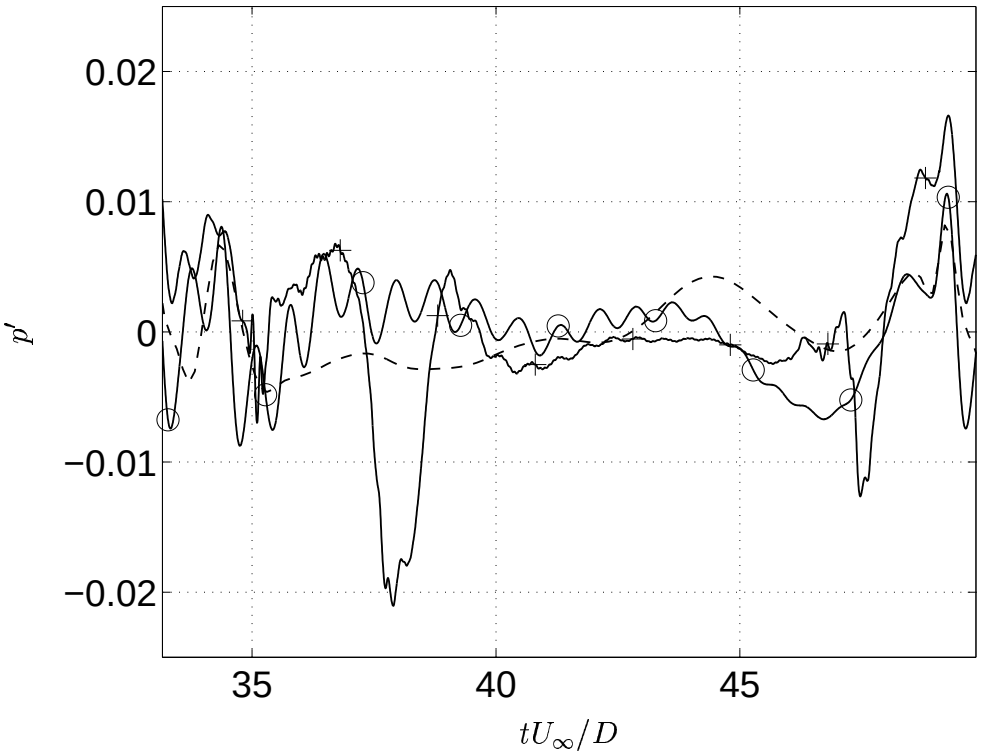

Figure 6.1: Acoustic pressure at observer seven using both dipole terms, Ref (−−), C1 (∘), C5 (+)

their individual contribution and their added effect in the same time frame. These results are shown in Fig. 6.2.

Figure 6.2 gives the acoustic signals using both source terms for three different sets of surface segments, where Region I contains the walls extending from the cavity leading edge to $14D$ downstream of this point except the cavity bottom, Region II contains the cavity bottom wall, and Total is the contribution for the whole region extending from the cavity leading edge to $14D$ downstream of this point. Figure 6.2 clearly shows that the total contribution is an effect of an almost complete cancellation of the sources at Region I and Region II. Both regions (I and II) show oscillations for the incompressible case, but the oscillations are small compared to the peak levels when treated individually. However, when combined (Total), the total pressure signal caused by the oscillations is almost as large as the resulting peak level. In fact, the amplitude of the oscillations increases when the two

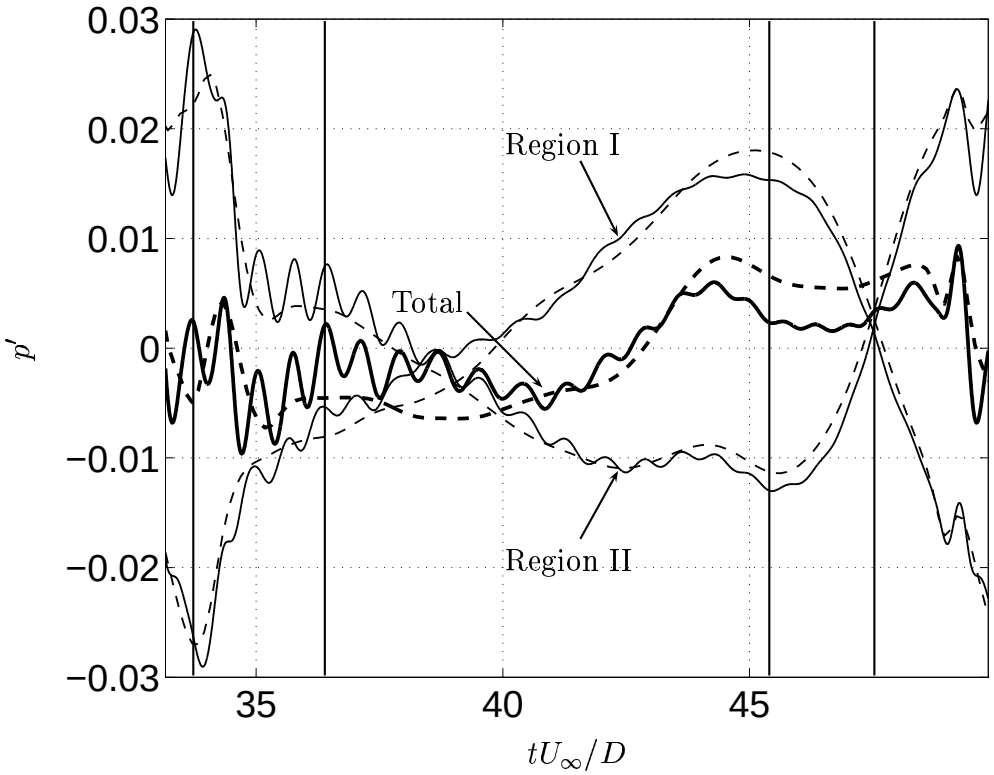

Figure 6.2: Acoustic signals at observer seven using both source terms, Region I (cavity leading edge to outlet except cavity bottom), Region II (cavity bottom), Total (cavity leading edge to outlet), Ref (−−), C1 (−)

surface regions are brought together since their phases match. Four vertical lines are also drawn in Fig. 6.2 representing instants in time when significant differences are found between the compressible and incompressible solutions. At the first instant, ($tU_\infty/D \approx 34$), a major mismatch occurs primarily due to an overprediction of the acoustic pressure at the cavity bottom wall for the incompressible case. At the second instant, ($tU_\infty/D \approx 36.5$), the incompressible signal is overpredicted primarily because of a phase match of the oscillation, but the level of the acoustic pressure is also overpredicted for both segments in the incompressible case. At the third instance, ($tU_\infty/D \approx 45.5$), the oscillations are small but the acoustic pressures for both surface segments are underpredicted in the incompressible case. At the final instance, ($tU_\infty/D \approx 47$), the underpredicted acoustic pressure found for the incompressible case causes a major error in the acoustic pressure.

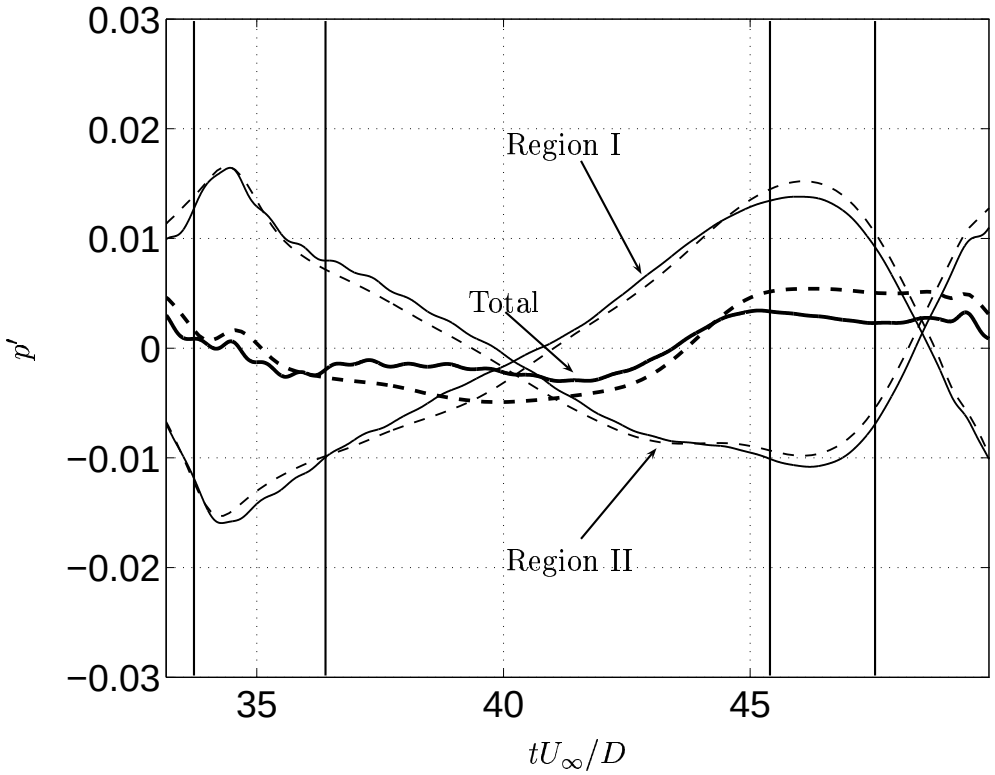

Figure 6.3: Acoustic signals at observer seven using source term one, Region I (cavity leading edge to outlet except cavity bottom), Region II (cavity bottom), Total (cavity leading edge to outlet), Ref (−−), C1 (−)

To check if one of the two source terms is possibly more prone to give the discrepancies in the acoustic signals, their contributions are plotted separately. Figure 6.3 shows the contributions from the first source term, i.e. the surface pressure term. The integration regions and observer are the same as in Fig. 6.2.

No major differences are present at the first two instants in time in Fig. 6.3, and the errors detected in Fig. 6.2 are therefore caused by the second source term. Major differences occur between instants two and three, however, and the offset is therefore primarily related to the first source term. At instant three the result in Fig. 6.3 points toward a combination of errors caused by both source terms if a comparison is made with Fig. 6.2. Instant four is, for the first source term, not located at the intersection between Region I and Region II signals; as Fig. 6.2 showed, the rapid change in signals is therefore

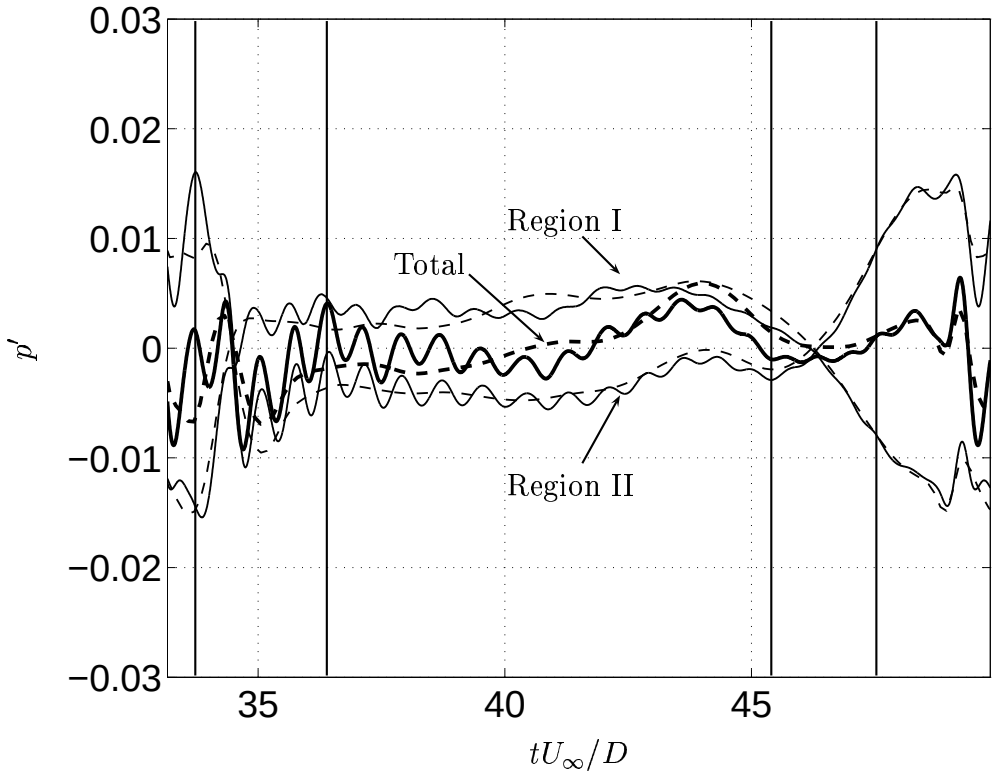

Figure 6.4: Wall segment contribution at observer seven, source term two

amplified by source term two. However, the difference between the two flow fields is mainly caused by source term one. In the final figure, Fig. 6.4, the corresponding results are shown for source term two.

Figure 6.4 supports the argument that the oscillations are due to the second source term. Errors in source term one were shown in Fig. 6.3 to be related to the intermediate and last part of the sequence. In contrast, the errors in source term two are instead related to the first part of the sequence. One cause of the results in the range $35 < tU_\infty/D < 40$ is synchronous oscillations that are amplified when brought together. One interesting finding is that the oscillations are more pronounced for the cavity bottom wall (Region II) as compared to Region I. The oscillations are therefore more probably caused by the cavity trailing edge. Further, at instant one, the difference detected in Fig. 6.2 occurs owing to a peak in source term two.

What then is the physical interpretation of the acoustic signals presented?

For a further analysis one must go back to the flow results given in Figs. 4(a) to 4(n) in Paper II. The peak levels between instant one and two in Fig. 6.3 corresponds approximately to Figs. 4(a) and 4(b) in Paper II. At this instant the main vortex has left the cavity, causing low pressure closest to the cavity trailing edge. At the cavity bottom, a new vortex is being generated at the cavity upstream wall. This vortex restricts the freestream flow from reaching the downstream part of the cavity bottom, which results in high pressure. Both these effects are identified in Fig. 6.3 at $tU_\infty/D \approx 34.5$, where Region I has its lowest value at the same time that Region II reaches its maximum value. After this occurence the flow starts to make a sharp, almost 90 degree directional change at the cavity trailing edge. Correspondingly, at $tU_\infty/D \approx 35$ the oscillations in the incompressible case, Fig. 6.4 are also found to be as highest. A compressible fluid can compensate for this by expanding, while an incompressible fluid can only balance between flow speed and pressure, and it is therefore most probable that the oscillations are caused by the singularity at the trailing edge. Studying the succeeding figures in Paper II, i.e Figs. 4(e) to 4(j), the change in the direction of the flow at the cavity trailing edge gradually becomes smaller and eventually vanishes. This corresponds well to the amplitude of the oscillations Fig. 6.4, which also gradually decays. At $tU_\infty/D \approx 46$, Region II reaches its maximum value, Fig. 6.3, and, correspondingly, Region I its minimum value. This instant corresponds approximately to Figs. 4(k) and 4(l) in Paper II, where stagnation occurs at approximately $0.1D$ downstream of the cavity trailing edge at the same time that the vortex starts to eject out of the cavity, causing low pressure at most downstream parts of the cavity bottom. The vortex will then be fully exposed to the freestream air which splits the vortex in two by the cavity trailing edge at the same time as it rapidly reduces in size. In a real fluid, the vortex will therefore be compressed, resulting in a slightly different pressure field at the most proximate walls as compared to an incompressible vortex.

This analysis gives strong indications that the trailing edge together with the incompressible treatment of the flow are the most probable causes of the present results, which cause oscillations in the pressure temporal derivative term as well as differences in the surface pressure term due to a different flow behavior. Since the noise emissions are mainly due to more or less complete cancellations of different sources, their representation is vital to obtaining acceptable results. It is therefore strongly recommended that a compressible description of the flow is used when considering noise radiation, at least for cases with rapid geometrical changes and few but strong flow structures.

Chapter 7

Summary of papers

7.1 Paper I

7.1.1 Motivation

This paper investigates both sound generation and radiation based on an incompressible approach by comparing an incompressible solution with a compressible direct simulation previously investigated by Larsson et al. [50, 53].

The case investigated is the laminar flow past an open two-dimensional cavity oscillating in wake mode with a depth to length ratio of $L/D = 4$ at the ambient Mach number of 0.15. Sound radiation is here computed from a temporal version of Curle's equation [49, 50]. It was shown in Larsson et al. [53] that the dipole terms were the most dominant source terms for this particular case, and therefore both sound generation and radiation are based on these source terms alone. The incompressible results are compared with the results obtained from a compressible flow field, and the investigation concerns spatial and temporal resolution as well as the extent of the computational domain for the incompressible cases.

7.1.2 Results

Concerning sound generation, all incompressible cases show good agreement over a major part of the existing walls. There exist two exceptions, however, the first relating to the inlet, where all incompressible cases overpredict the pressure temporal derivative term, most probably owing to the boundary condition applied and the second close to the outlet, where all incompressible cases show major overpredictions of both source terms. The cause of this latter overprediction is the convection of strong vortices over the outlet, causing local backflow, which results in pressure perturbations contaminating the source signals. Concerning sound radiation, the directivity is evaluated at nine observers equally distributed $7.18D$ above the cavity. A perfect match is found when the surface integral is restricted to the cavity walls alone. Inclusion of the wall extending from the inlet to the cavity leading edge to the former integration surfaces gives an overprediction of the incompressible cases and highlights the issues detected at the inlet. Adding segments of the wall extending from the cavity trailing edge to the outlet increases the discrepancies in the directivity obtained from the different cases and points toward reflections caused by the outlet. The best agreement is found for the case with the lowest resolution, hinting at a resolution issue at the cavity trailing edge. It is believed that the results could be significantly improved by preventing backflow from occuring at the outlet.

7.2 Paper II

7.2.1 Motivation

Paper I highlighted two possible problems in using incompressible sources in the modified version of Curle's equation. The first relates to the boundary conditions traditionally used in incompressible flow simulations, which may pollute the acoustic source terms, especially for flows with strong structures that may cause backflow when convected over the outlet. The second problem concerns a more severe aspect of using incompressible flow fields for pitched flow-induced noise and could be caused by a small phase shift due to the neglected compressibility of the fluid.

Here, the first aspect is further investigated by shifting the outlet boundary

condition. The present technique, referred to as buffer zones, adds dissipative source terms to the governing momentum equations.

7.2.2 Results

By using buffer zones at the outlet, the overprediction in noise levels is reduced by about 3 [dB] for the observers located furthest downstream. Still, significant discrepancies in noise levels exist for most observers, which is further analyzed by splitting the surfaces into several segments and separately analyzing their individual contributions. The general conclusion made in this paper points at a potential problem in using incompressible sources to compute the acoustics in the temporal form of Curle's equation. It is shown that the wall extending from the cavity trailing edge to the outlet alone gave identical directivity for the compressible and the incompressible flow field. Adding the upstream and downstream cavity walls to the surface integration also gave an almost perfect match in directivity. However, when the cavity bottom wall was added to the surface integration, a major mismatch in the directivity was found.

7.3 Paper III

7.3.1 Motivation

The incompressible approach can successfully be used to predict the magnitude of the dipole source terms in Curle's equation. This conclusion was drawn in the first two papers but was validated only for the laminar flow past a two-dimensional cavity. To check whether this conclusion is also true for more complex geometries and flow conditions, the next case concerns the flow past a generic side mirror mounted on a flat plate. This case has been the subject of several previous studies [11, 55–58]. The main motivations for the present study were as follows: to investigate the correlation of surface pressure fluctuations between measurements and simulations; to present the best practice approach in terms of turbulence modeling, choice of advection scheme and near-wall treatment; and to give recommendations regarding resolution. A parameter study was therefore conducted to predict both flow

properties and sound generation.

7.3.2 Results

Both the upwind biased advection scheme and the bounded central schemes predict the pressure fluctuations at equal levels when LES is used. However, the upwind biased scheme is found to be more sensitive to the turbulence model than the bounded central scheme. The dynamic Smagorinsky model shows tendencies to oscillate in the mirror wake, and the DES model is too dissipative, at least in the near wake, which means that the best candidate among the turbulence models investigated is the Smagorinsky-Lilly model. A rule of thumb estimate for predicting the grid cut-off in the pressure fluctuation spectra was given and was supported by the experimental results.

7.4 Paper IV

7.4.1 Motivation

The main motivation for Paper IV concerns the prediction of the two dipole terms in the temporal formulation of Curle's equation for a representative ground vehicle. To the author's knowledge, no studies have been conducted in which these two source terms are evaluated quantitatively against measurements. This paper thus investigates the degree to which these two source terms can be predicted by using wall functions and hex-dominant meshes with isotropic resolution boxes in the regions with separated flow. The best practice guidelines from Paper III were applied. In addition to the prediction of the acoustic source terms, flow measurements were carried out to some extent to verify mean flow quantities. Two different mesh approaches were investigated, one with two prism layers closest to the surface and another in which the prisms were replaced by trimmed cells. In the second approach the near wall resolution was compensated for by both higher surface resolution and increased resolution in regions of separated flow.

7.4.2 Results

It was shown that all simulations accurately predict the magnitude of the velocity closest to the front side window. Some variations in the size and shape of the mirror recirculation zone were found between the different grids, most probably due to differences in the flow detachment point at the mirror head boundary layer. Concerning the acoustic source terms, both terms are well predicted up to about 1000 [Hz] in at least one of the three simulations. This finding applies for most locations. At three locations, major discrepancies were found and were hypothetically argued to be caused by small differences in the local flow pattern. The near-wall cell topology in attached flow regions is crucial to capturing the downstream source terms since they are mainly influenced by flow separations. Highest source levels are found at the lower part of the A pillar, the near wake of the mirror foot and the vortex flow at the front side window caused by the A pillar. These regions are of highest importance to the air-rush noise levels in the compartment since, these regions are most probable to contain leaks, and their proximity to the drivers ear position.

Chapter 8

Concluding Remarks

Three different cases were investigated to seek answers to the research hypotheses formulated in Chapter 1. Thus the question addressed is whether these hypotheses have been answered:

Hypothesis 1, *Is the assumption of incompressibility justified for low Mach number, wall-bounded flows where the hydrodynamics is the dominating cause of the noise generation?*

All the cases studied in this thesis show that the RMS levels of the two source terms in the temporal formulation of Curle's equation can be accurately predicted by using the incompressible approach. An estimate for predicting the local grid cut-off is presented by relating the magnitude of the velocity fluctuation with the near-wall grid spacing. Using this relation, the upper frequency limit for the first source term can be estimated and has been shown to be supported by the measurements. Most important for the level and location of the two dipole sources investigated is the wall normal grid spacing. However, for both the generic side mirror and the generic SUV, it seems as though the law-of-the-wall can be used without compromising the accuracy of the acoustic source results.

As concerns sound radiation from an incompressible flow, indications are given that there are several aspects that are more or less severe in using the incompressible approach. These are:

- The pressure in the incompressible flow equations is elliptic. This means that distortions will more or less be present in the whole domain at the same instant as they occur. In the open cavity case such distortions were found to be caused primarily by the outlet. Since they will match in phase over the integration surfaces, it is probable that their effect will be amplified at an observer.
- Singularities in the mesh caused by sharp edges can also cause oscillations since an incompressible fluid can only compensate for sharp directional changes by increasing the flow speed or decreasing the pressure.
- Rapid changes in the geometry will cause a compression or expansion of the flow when treated as compressible. These effects will be lost when the fluid is assumed to be incompressible. Possible effects are small changes in the pressure field, which may generate errors in the acoustic signals for flows with few dominant structures.

Hypothesis 2, *Do the surface pressure terms provide sufficient information to evaluate the radiated sound in a representative vehicle where air-rush noise is our main concern?*

It is shown for a production vehicle that the compartment noise scales almost perfectly with dipoles. Thus it may be sufficient to restrict the sources to the two main dipole terms; however, this should be investigated further owing to the sensitivity of the acoustic integral equations. With this information it is at least theoretically possible to proceed with noise transmission through the vehicle structures to the final goal of obtaining the noise levels in the compartment.

Hypothesis 3, *Can a method be established to at least qualitatively predict air-rush noise for a production vehicle fulfilling the industrial needs of both robustness and accuracy?*

This thesis demonstrates how acoustic sources caused by the vehicle external flow can be predicted from unsteady flow simulations. The size, location and level of these sources can be used to reduce the air-rush noise for regions were sealing and structural properties are particularily important. Additionally, this information can be used to give both suggestions for geometrical changes and to evaluate different styling proposals in the early phases of the vehicle programs.

Chapter 9

Suggestions for further work

- Investigations of an implicit compressible approach based on the existing and more stable velocity-pressure coupling algorithms are suggested, when sound radiation is the main concern. By using a convective CFL number as a criterion for determining the time step size, the computational effort will be comparable to an incompressible simulation but will probably result in the loss of the reflection contribution, similar to the incompressible approach. With this approach, buffer zones can also be used in a more effective and less flow-affecting way.
- Methods should be investigated for transmitting the excitations over the exterior through primarily the windows. If the transmission spectra are known in advance, the acoustic sources may be filtered and the new, corrected source field could then be used to propagate the noise in the vehicle compartment.
- Low pass filtering of the acoustic source may be successful and could be investigated, since high frequency noise caused by unresolved turbulence will probably create problems when used in the acoustic integral equations.

Bibliography

[1] J.R. Thomson. Wind noise - a practical approach. Society of Automotive Engineers, 840B, March 30 - April 3, 1964.

[2] W.R. Stapleford and G.W. Carr. Aerodynamic noise in road vehicles, part 1: The relationship between aerodynamic noise and the nature of the airflow. The Motor Industry Research Association, 1971/2, November, 1970.

[3] G.F. Romberg and R.G. Lajoie. An objective method of estimating car interior aerodynamic noise. Society of Automotive Engineering,770393, 1977.

[4] R. Buchheim, W. Dobrzynski, H. Mankau, and D. Schwabe. Vehicle interior noise related to external aerodynamics. *International Journal of Vehicle Design*, 3, 1982.

[5] A.R. George. Automobile aerodynamic noise. Society of Automotive Engineers, 900315, February 26 - March 2, 1990.

[6] T.H.L. Lounsberry, M.E. Gleason, and M.M. Puskarz. Laminar flow whistle on a vehicle side mirror. *Society of Automotive Engineering*, pages 2007–01–1549, 2007.

[7] W.R. Stapleford. Aerodynamic noise in road vehicles, part 2: A study of the sources and significance of aerodynamic noise in saloon cars. The Motor Industry Research Association, 1972/6, November, 1970.

[8] M. Watanabe, M. Harita, and E. Hayashi. The effect of body shapes on wind noise. Society of Automotive Engineers, 780266, 1978.

[9] A. Lorea, V. Castelluccio, A. Costelli, and M. Masoero. A wind-tunnel method for evaluating the aerodynamic noise of cars. Society of Automotive Engineering, 860215, 1986.

[10] K. Ono, R. Himeno, and T. Fukushima. Prediction of wind noise radiated from passenger cars and its evaluation based on auralization. *Journal of Wind Engineering and Industrial Aerodynamics*, 88:403–419, 1999.

[11] T. Rung, D. Eschricht, J. Yan, and F. Thiele. Sound radiation of the vortex flow past a generic side mirror. 8th AIAA/CEAS Aeroacoustics Conference. Breckenridge, Colorado, AIAA-2002-2340, 17-19 June, 2002.

[12] J.E. Ffowcs Williams and D.L. Hawkings. Sound generation by turbulence and surfaces in arbitrary motion. *Philos. Trans. Roy. Soc.*, A 264 No. 1151:321–342, 1969.

[13] H. Posson and F. Pérot. Far-field evaluation of the noise radiated by a side mirror using les and acoustic analogy. 2th AIAA/CEAS Aeroacoustics Conference. Cambridge, Massachusetts, AIAA-2006-2719, 8-10 May, 2006.

[14] B.D. Duncan, R. Sengupta, S. Mallick, R. Shock, and D.B. Sims-Williams. Numerical simulation and spectral analysis of pressure fluctuations in vehicle aerodynamic noise generation. Society of Automotive Engineering, 2002-01-0597, 2002.

[15] S. Senthooran, B. Crouse, S. Noelting, D. Freed, D.B. Duncan, G. Balasubramanian, and R.E. Powell. Prediction of wall pressure fluctuations on an autombile side-glass using a lattice-boltzmann method. AIAA/CEAS Aeroacoustics Conference and Exhibit, Cambridge, Massachusetts, 2006-2559, 8-10 May, 2006.

[16] A. Gaylard. CFD simulation of side glass surface noise spectra for a bluff suv. Society of Automotive Engineering, 2006-01-0137, 2006.

[17] DR. Chapman. Computational aerodynamics development and outlook. *AIAA Journal*, 17:1293–1313, 1979.

[18] L. Temmerman, M. Hadziabdic, M.A. Leschziner, and K. Hanjalic. A hybrid two-layer URANS-LES approach for large eddy simulation at high reynolds number. *International Journal of Heat and Fluid Flow*, 26:173–190, 2005.

[19] P. Spalart. Strategies for turbulence modelling and simulations. *International Journal of Heat and Fluid Flow*, 21:252–263, 2000.

[20] F. Nicoud, J.S. Baggett, P. Moin, and W. Cabot. Large eddy simulation wall-modeling based on suboptimal control theory and linear stochastic estimation. *Physics of Fluids*, 13(10):2968–2984, 2001.

[21] L. Davidson and S. Dahlström. Hybrid LES-RANS: An approach to make LES applicable at high Reynolds number. In *ICHMT International Symposium on Advances in Computational Heat Transfer*, 2004.

[22] C.D. Wilcox. *Turbulence modeling for CFD; Second edition.* DCW Industries, 1998.

[23] T.J. Craft, S.E. Gant, H. Iavocides, and B.E. Launder. A new wall function strategy for complex turbulent flows. *Numerical Heat Transfer*, B(45):301–318, 2004.

[24] E. Balaras and C. Benocci. Two-layer approximate boundary conditions for large-eddy simulations. *AIAA Journal*, 34(6):1111–1119, 1996.

[25] W. Cabot and P. Moin. Approximate wall boundary condition in the large-eddy simulation of high Reynolds number flow. *Flow, Turbulence and Combustion*, 63:269–291, 1999.

[26] M. Wang and P. Moin. Dynamic wall modeling for large-eddy simulation of complex turbulent flows. *Physics of Fluids*, 14(7):2043–2051, 2002.

[27] L. Davidson and S.H. Peng. Hybrid LES-RANS modeling: A one equation SGS model combined with a k-ω model for predicting recirculating flows. *International Journal for Numerical Methods in Fluids*, 00:1-6, 2000.

[28] P.G. Tucker and L. Davidson. Zonal $k - l$ based large eddy simulation. *Computers and Fluids*, 33:267–287, 2004.

[29] F. Hamba. A hybrid RANS/LES simulation of turbulent channel flow. *Theoretical Computational Fluid Dynamics*, 16:387–403, 2003.

[30] L. Davidson and M. Billson. Hybrid LES-RANS using synthesized turbulent fluctuations for forcing in the interface region. *Submitted, International Journal of Heat and Fluid Flows*, 2005.

[31] E. Labourasse and P. Sagaut. Reconstruction of turbulent fluctuations using a hybrid RANS/LES approach. *Journal of Computational Physics*, 182:301–336, 2002.

[32] P. Spalart, W-H. Jou, M. Strelets, and S.R. Allmaras. Comments on the feasibility of LES for wings, and on a hybrid RANS/LES approach. In *1st AFOSR International conference on DNS/LES. In advances in DNS/LES*, pages 137–147, 1997.

[33] S. Schmidt and F. Thiele. Detached eddy simulation of flow around A-airfoil. *Flow, Turbulence and Combustion*, 71:261–278, 2003.

[34] A. Travin, M. Shur, M. Strelets, and P Spalart. Detached-eddy simulations past a circular cylinder. *Flow, Turbulence and Combustion*, 63:293–313, 1999.

[35] G.S. Constantinescu and K.D. Squires. LES and DES investigations of turbulent flow over a sphere at Re=10000. *Flow, Turbulence and Combustion*, 70:267–298, 2003.

[36] G.S. Constantinescu and K.D. Squires. Numerical investigations of flow over a sphere in the subcritical and supercritical regimes. *Physics of Fluids*, 16:1449–1466, 2004.

[37] L.S. Hedges, A.K. Travin, and P. Spalart. Detached-eddy simulations over a simplified landing gear. *Journal of Fluids Engineering*, 124:413–423, 2002.

[38] P.G. Tucker. Differential equation-based wall distance computation for DES and RANS. *Journal of Computational Physics*, 190:229–248, 2003.

[39] V.N. Vatsa and B.A Singer. Evaluation of a second-order accurate Navier-Stokes code for detached eddy simulation past a circular cylinder. 21th AIAA Aerospace Sciences Meeting and Exhibit. Reno, NV, AIAA-2001-0879, 8-11 January, 2001.

[40] F. Menter, M. Kuntz, and R. Bender. A scale-adaptive simulation model for turbulent flow predictions. 41st Aerospace Science Meeting and Exhibit, AIAA-2003-0767, 6-9 January, 2003.

[41] F. Menter and Y. Egorov. A scale-adaptive simulation model using two-equation models. AIAA-2005-1095, 2005.

[42] C.G. Speziale. Turbulence modeling for time-dependent RANS and VLES, a review. *AIAA Journal*, 36(2):173–184, 1998.

[43] P. Batten, U. Goldberg, and S. Chakravarthy. LNS-an approach towards embedded LES. 40th AIAA Aerospace Sciences Meeting and Exhibit, AIAA-2002-0427, 14-17 January, 2002.

[44] P. Batten, U. Goldberg, and S. Chakravarthy. Interfacing statistical turbulence closures with large-eddy simulations. *AIAA Journal*, 42(3):485–492, 2004.

[45] H. Tennekes and J.L. Lumley. *A first course in turbulence.* The MIT Press, 1972.

[46] S. Sarkar and M.Y. Hussaini. Computation of the acoustic radiation from bounded homogeneous flows. *Computational Aero Acoustics*, pages 335–354, 1993.

[47] N. Andersson. *A study of subsonic turbulent jets and their radiated sound using Large-Eddy Simulation.* PhD thesis, Chalmers University of Technology, 2005.

[48] P.M. Morse and H. Feshbach. *Methods of theoretical physics, Volume I.* McGraw-Hill Book Company, Inc, 1953.

[49] N. Curle. The influence of solid boundaries upon aerodynamic sound. *Proc. Roy. Soc*, A231:505–514, 1955.

[50] J. Larsson. *Computational aero acoustics for vehicle applications.* PhD thesis, Chalmers University of Technology, 2002.

[51] D.G. Crighton. Basic principles of aerodynamic noise generation. *Prog. Aerospace Sci.*, 16:31–96, 1975.

[52] L. Davidson and B. Farhanieh. Calc-bfc, a finite-volume code employing collocated variable arrangement and cartesian velocity components for computation of fluid flow and heat transfer in complex three-dimensional geometries. Chalmers University of Technology, Department of Thermo and Fluid Dynamics, 1995.

[53] J. Larsson, L. Davidson, M. Olsson, and L.E. Eriksson. Aero acoustic investigation of an open cavity at low Mach number. *AIAA Journal*, 42(12):2462–2473, 2004.

[54] C.K.W. Tam and J.C. Webb. Dispersion-relation-preserving finite difference schemes for computational acoustics. *Journal of Computational Physics*, 107:262–281, 1993.

[55] R. Höld, A. Brenneis, and A. Eberle. Numerical simulation of aeroacoustic sound generated by generic bodies placed on a plate: Part I - prediction of aeroacoustic sources. 5th AIAA/CEAS Aeroacoustics Conference. Seattle, Washington, AIAA-99-1896, 10-12 May 1999.

[56] R. Siegert, V. Schwartz, and J. Reichenberger. Numerical simulation of aeroacoustic sound generated by generic bodies placed on a plate: Part II - prediction of radiated sound pressure. 5th AIAA/CEAS Aeroacoustics Conference. Seattle, Washington, AIAA-99-1895, 10-12 May 1999.

[57] EXA Consortium. Validation update: Model mirror. Aeroacoustic Consortium 2003/2004 Presentation, 20 August, 2003.

[58] L. Bipin, S. Sandeep, and X. Jieyong. Computational aeroacoustic analysis of a generic side view mirror. Noise and Vibration Conference and Exhibition. Traverse City, Michigan, SAE-2003-01-1698, 5-8 May, 2003.

[59] M.J. Lighthill. On sound generated aerodynamically,I. general theory. *Proc. Roy. Soc.*, A 211:564–587, 1952.

[60] D.J Tritton. *Physical Fluid Dynamics.* Oxford Science Publications, 1988.

Appendix A

Order of magnitude estimation of the different source types

The following text is partly covered by the work of Crighton [51].

A common attribute in the work done on aero acoustic scaling laws is a farfield perspective and assumptions that may not be true for automotive applications. This raised the need to review the order of magnitude estimation in flow-induced wind noise for ground vehicles with a special emphasis on the noise caused by the side mirror at cruising conditions. The starting point for the order of magnitude estimates in the following sections originates from the space formulation of Ffowcs Williams and Hawking's equation [12], which can be written as follows, Larsson [50]:

$$\begin{aligned}\rho(\mathbf{x},t)-\rho_o &= \frac{1}{4\pi a_\infty^2}\frac{\partial^2}{\partial x_i \partial x_j}\int_V \frac{T_{ij}'^*}{r(1-\frac{l_j v_j}{a_\infty})}dV(\mathbf{y}^*) \\ &\quad -\frac{1}{4\pi a_\infty^2}\frac{\partial}{\partial x_i}\int_S \frac{F_i^*}{r(1-\frac{l_j v_j}{a_\infty})}dS(\mathbf{y}^*) \\ &\quad +\frac{1}{4\pi a_\infty^2}\frac{\partial}{\partial t}\int_S \frac{Q^*}{r(1-\frac{l_j v_j}{a_\infty})}dS(\mathbf{y}^*) \end{aligned} \tag{A.1}$$

$$\begin{aligned} T_{ij}'^* &= \rho(u_i^*+v_i)(u_j^*+v_j)-\tau_{ij}^*+\left(p-a_\infty^2(\rho-\rho_\infty)\right)\delta_{ij} \\ F_i^* &= \left(\rho(u_i^*+v_i)u_j^*+p\delta_{ij}-\tau_{ij}^*\right)n_j \\ Q^* &= \left(\rho_\infty v_i+\rho u_i^*\right)n_i \end{aligned} \tag{A.2}$$

In Eq. A.1, $T_{ij}'^{*}$ represents the quadrupoles or stresses in the fluid. Due to the more general validity of the theory as compared to, for example, Lighthill [59], it can also handle the flow around bodies, where F_i^* represents the dipoles or fluctuating forces on the surfaces and Q^* represents fluctuating mass fluxes through the surfaces. The flow-exposed body may move with surface velocity v_i as compared to flow velocity u_i^*. Equation A.1 is further expressed in a coordinate system, $\mathbf{y}^*$, moving with constant velocity, v_i, relative $\mathbf{y}$, according to $y_i = y_i^* + v_i\tau$.

Before deriving the order of magnitude estimates for the different sources, some definitions are presented to avoid repetitive work. Central to the shift from space to time in Eq. A.1 is the retarded time, τ, which is the time the source dynamics are evaluated as compared to the observer time, t. The time lag between the source and observer depends on the speed of sound, a_∞, and the distance between them, $r = |x_i - y_i|$, where x_i represents the observer location and y_i represents the source location. The source time or retarded time is defined as

$$\tau = t - \frac{r}{a_\infty} \tag{A.3}$$

The distance between the source and the observer, r, can also be expressed as the space lag between the source and observer according to

$$r = (t - \tau)a_\infty \tag{A.4}$$

Differentiation of r with respect to τ gives

$$\frac{\partial r}{\partial \tau} = -a_\infty \tag{A.5}$$

In the dipole and quadrupole sections, the differentiation of τ with respect to the observer location, x_i, is needed, which gives

$$\frac{\partial \tau}{\partial x_i} = -\frac{1}{a_\infty}\frac{\partial r}{\partial x_i} \tag{A.6}$$

where

$$\frac{\partial r}{\partial x_i} = \frac{x_i - y_i}{|x_i - y_i|} = l_i \tag{A.7}$$

Differentiation of the directional vector, l_i, with respect to the observer location gives

$$\frac{\partial l_j}{\partial x_i} = \frac{\partial}{\partial x_i}\left(\frac{x_j - y_j}{r}\right) = \frac{\frac{\partial x_j}{\partial x_i} r - (x_j - y_j)\frac{x_i - y_i}{|x_i - y_i|}}{r^2} = \frac{\delta_{ij} - l_i l_j}{r} \tag{A.8}$$

A.1 Monopole dominant source fields

We start with the most elementary source type, monopoles. If this source type is the dominating source term, Ffowcs-Williams and Hawking's equation, Eq.A.1, reduces to

$$p'(\mathbf{x},t) \approx \frac{1}{4\pi}\frac{\partial}{\partial t}\int_S \left[\frac{(\rho_\infty v_i + \rho u_i^*)\, n_i}{r(1-\frac{l_j v_j}{a_\infty})}\right] dS(\mathbf{y}^*) \tag{A.9}$$

Compared to Eq. A.1, the terms in brackets in Eq. A.9 simply emphasizes that they are to be evaluated at retarded time. For permeable surfaces in a fixed coordinate frame, Eq. A.9 reduces to

$$p'(\mathbf{x},t) = \frac{1}{4\pi}\frac{\partial}{\partial t}\int_S \left[\frac{\rho u_i n_i}{r}\right] dS(\mathbf{y}) \tag{A.10}$$

Eq. A.10 states that each source point $\mathbf{y}$ is evaluated at retarded time. If l_m is a representative length scale of the source region and u_m is a velocity scale for the surface normal fluctuation, then the maximum difference in emission times over a surface l_m^2 is of the order l_m/a_∞. Further, if this maximum difference in emission times is significantly larger than l_m/u_m, or in other words $Ma_m << 1$, then the emission times are unimportant and may be replaced by $\tau \approx t - |\mathbf{x}|/a_\infty$ as compared to $\tau = t - r/a_\infty$. It is here implicitly assumed that the coordinate system is placed at the center of the source region. The denominator can then be taken outside the surface integration, which results in

$$p'(\mathbf{x},t) \approx \frac{1}{4\pi|\mathbf{x}|}\frac{\partial}{\partial t}\int_S [\rho u_i n_i]\, dS(\mathbf{y}) \tag{A.11}$$

If we assume that temperature deviations from the ambient state are small, then the density can be approximated as $\rho \approx \rho_\infty$. Using the source length scale l_m and the time scale, which we, for now, write as l_m/u_m, then the source frequency can be expressed as $\frac{\partial}{\partial t} \propto u_m/l_m$, which results in the following order of magnitude estimate.

$$p'(\mathbf{x},t) \propto \rho_\infty u_m^2 \frac{l_m}{|\mathbf{x}|} \tag{A.12}$$

A.2 Dipole dominant source fields

The second level of sources are dipoles. If they are the main contributor to the radiated noise, Eq. A.1 reduces to

$$p'(\mathbf{x},t) \approx -\frac{1}{4\pi}\frac{\partial}{\partial x_i}\int_S \left[\frac{\left(\rho(u_i^*+v_i)u_j^*+p\delta_{ij}-\tau_{ij}^*\right)n_j}{r(1-\frac{l_j v_j}{a_\infty})}\right] dS(\mathbf{y}^*) \qquad \text{(A.13)}$$

If we again assume stationary walls $v_i = 0$ in a fixed coordinate frame, high Reynolds number, then the dominating term in Eq. A.13 will be the pressure term.

$$p'(\mathbf{x},t) \approx -\frac{1}{4\pi}\frac{\partial}{\partial x_i}\int_S \left[\frac{pn_i}{r}\right] dS(\mathbf{y}) \qquad \text{(A.14)}$$

The surface integral is independent of x_i and can be taken inside the integral, which gives

$$p'(\mathbf{x},t) \approx -\frac{1}{4\pi}\int_S \frac{\partial}{\partial x_i}\left[\frac{pn_i}{r}\right] dS(\mathbf{y}) \qquad \text{(A.15)}$$

Using the chain rule ($\frac{\partial}{\partial x_i} = \frac{\partial \tau}{\partial x_i}\frac{\partial}{\partial \tau}$) in Eq. A.15 and carrying out the differentiation with respect to time gives

$$p'(\mathbf{x},t) \approx -\frac{1}{4\pi}\int_S \frac{\partial \tau}{\partial x_i}\left[\frac{\frac{\partial p}{\partial \tau}r - p\frac{\partial r}{\partial \tau}}{r^2}n_i\right] dS(\mathbf{y}) \qquad \text{(A.16)}$$

Replacing $\frac{\partial p}{\partial \tau}$ with $\dot{p}$ to simplify the notation and replacing the derivatives according to Eqs. A.5, A.6 and A.7 gives the final expression

$$p'(\mathbf{x},t) \approx \frac{1}{4\pi a_\infty}\int_S l_i\left[\frac{\dot{p}}{r}n_i\right] dS(\mathbf{y}) + \frac{1}{4\pi}\int_S l_i\left[\frac{p}{r^2}n_i\right] dS(\mathbf{y}) \qquad \text{(A.17)}$$

Instead of one term for the monopoles, we now have two terms. If we in a similar manner as before approximate $\frac{\partial}{\partial \tau} \propto u_d/l_d$ and $p \propto \rho_0 u_d^2$, this gives

$$p'(\mathbf{x},t) \propto \rho_\infty u_d^2 \frac{l_d}{|\mathbf{x}|}\left(Ma_d + \frac{l_d}{|\mathbf{x}|}\right) \qquad \text{(A.18)}$$

Equation A.18 now consists of two terms that differ by a factor of $|\mathbf{x}|Ma_d/l_d$. Both terms are dipole terms and it is clear that detailed information about

the source is needed to sort out the largest term of the two. The traditional way of finding this dominant term is to have a farfield perspective where only terms involving $\mathcal{O}(|\mathbf{x}|^{-1})$ (i.e. the first term in Eq. A.18) are retained. In a ground vehicle point of view where the interior noise is our main concern, this may not be true and a different approach is needed. Instead we relate $\frac{\partial}{\partial \tau} \sim \omega$ in Eq. A.17, where $\omega = 2\pi f$, and where f is the frequency of the emitted noise. This choice is based on the idea that frequency and time are related through $e^{-i2\pi ft}$. We then obtain the following estimate

$$p'(\mathbf{x},t) \propto \rho_\infty u_d^2 \frac{l_d}{|\mathbf{x}|}\left(\frac{l_d 2\pi f}{a_\infty} + \frac{l_d}{|\mathbf{x}|}\right) \tag{A.19}$$

The two terms now differ by a factor of $2\pi f|\mathbf{x}|/a_\infty$. Wind noise dominates in the frequency range $500 < f < 5000$[Hz], and the driver of the vehicle is located in the order of 1 [m] from the side mirror source field. In the lower limit of 500 [Hz], this gives that the first term is approximately one order of magnitude larger than the second term. For the frequency range of interest, this means that radiated sound can be approximated as

$$p'(\mathbf{x},t) \propto \rho_\infty u_d^2 \frac{l_d}{|\mathbf{x}|} M a_d \tag{A.20}$$

A.3 Quadrupole dominant source fields

For a quadrupole dominant sound field, Eq. A.1 reduces to

$$p'(\mathbf{x},t) \approx \frac{1}{4\pi}\frac{\partial^2}{\partial x_i \partial x_j}\int_V \left[\frac{T_{ij}}{r}\right] dV(\mathbf{y}) \tag{A.21}$$

where

$$T_{ij} \;=\; \rho u_i u_j - \tau_{ij} + \left(p - a_\infty^2(\rho - \rho_\infty)\right)\delta_{ij} \tag{A.22}$$

Moving the first derivative inside the integral and using the chain rule gives

$$p'(\mathbf{x},t) = \frac{1}{4\pi}\frac{\partial}{\partial x_i}\int_V \frac{\partial \tau}{\partial x_j}\left[\frac{\partial}{\partial \tau}\frac{T_{ij}}{r}\right] dV(\mathbf{y}) \tag{A.23}$$

Conducting the time differentiation and using Eqs. A.6, A.7 and A.5 in Eq. A.23 gives

$$p'(\mathbf{x},t) = -\frac{1}{4\pi}\frac{\partial}{\partial x_i}\int_V l_j\left[\frac{\dot{T}_{ij}}{a_\infty r}+\frac{T_{ij}}{r^2}\right]dV(\mathbf{y}) \tag{A.24}$$

The second observer derivative is now moved inside the volume integral.

$$p'(\mathbf{x},t) = -\frac{1}{4\pi}\int_V \frac{\partial}{\partial x_i} l_j\left[\left(\frac{\dot{T}_{ij}}{a_\infty r}+\frac{T_{ij}}{r^2}\right)\right]dV(\mathbf{y}) \tag{A.25}$$

Differentiation of products gives

$$p'(\mathbf{x},t) = -\frac{1}{4\pi}\int_V \left[\frac{\partial l_j}{\partial x_i}\left(\frac{\dot{T}_{ij}}{a_\infty r}+\frac{T_{ij}}{r^2}\right)+l_j\frac{\partial}{\partial x_i}\left(\frac{\dot{T}_{ij}}{a_\infty r}+\frac{T_{ij}}{r^2}\right)\right]dV(\mathbf{y}) \tag{A.26}$$

Applying Eq. A.8 to Eq. A.26 and the chain rule for the second term gives

$$\begin{aligned} p'(\mathbf{x},t) &= -\frac{1}{4\pi}\int_V \left[\frac{\delta_{ij}-l_il_j}{r}\left(\frac{\dot{T}_{ij}}{a_\infty r}+\frac{T_{ij}}{r^2}\right)\right. \\ &\quad \left. + l_j\frac{\partial\tau}{\partial x_i}\frac{\partial}{\partial\tau}\left(\frac{\dot{T}_{ij}}{a_\infty r}+\frac{T_{ij}}{r^2}\right)\right]dV(\mathbf{y}) \end{aligned} \tag{A.27}$$

Carrying out the time differentiation for the second term gives

$$\begin{aligned} p'(\mathbf{x},t) &= -\frac{1}{4\pi}\int_V \left[\frac{\delta_{ij}-l_il_j}{r}\left(\frac{\dot{T}_{ij}}{a_\infty r}+\frac{T_{ij}}{r^2}\right)\right. \\ &+ \left. l_j\frac{\partial\tau}{\partial x_i}\left(\frac{\ddot{T}_{ij}r+\dot{T}_{ij}a_\infty}{a_\infty r^2}+\frac{\dot{T}_{ij}r+2T_{ij}a_\infty}{r^3}\right)\right]dV(\mathbf{y}) \end{aligned} \tag{A.28}$$

Inserting Eqs. A.6 and A.7 in Eq. A.28 and rearranging the terms gives

$$\begin{aligned} p'(\mathbf{x},t) &= \\ &\frac{1}{4\pi}\int_V\left[\frac{l_il_j}{a_\infty^2 r}\ddot{T}_{ij}+\frac{3l_il_j-\delta_{ij}}{a_\infty r^2}\dot{T}_{ij}+\frac{3l_il_j-\delta_{ij}}{r^3}T_{ij}\right]dV(\mathbf{y}) \end{aligned} \tag{A.29}$$

At high Reynolds number and for flows where temperature deviations from uniformity are small, the main sound generator in the Lighthill stress tensor is the momentum flux tensor, i.e. $T_{ij}\approx\rho_\infty u_iu_j$. The radiated sound can then be approximated as

$$\begin{aligned} p'(\mathbf{x},t) &= \frac{\rho_\infty}{4\pi}\int_V\left[\frac{l_il_j}{a_\infty^2 r}\frac{\partial^2}{\partial t^2}u_iu_j\right. \\ &+ \left.\frac{3l_il_j-\delta_{ij}}{a_\infty r^2}\frac{\partial}{\partial t}u_iu_j+\frac{3l_il_j-\delta_{ij}}{r^3}u_iu_j\right]dV(\mathbf{y}) \end{aligned} \tag{A.30}$$

Using similar approximations as for the dipoles and monopoles gives

$$p'(\mathbf{x},t) \quad \propto \quad \rho_\infty u_q^2 \frac{l_q}{|\mathbf{x}|}\left(Ma_q^2 + \frac{l_q}{|\mathbf{x}|}Ma_q + \frac{l_q^2}{|\mathbf{x}|^2}\right) \tag{A.31}$$

If we make the approximation that $|\mathbf{x}| \approx 1$ [m], that a typical length scale of the source region is about 0.1 [m] and that the source Mach number is in the order of $Ma_q \approx 0.1$, all terms are of same magnitude. In a similar manner as before, we start from Eq. A.30 and approximate $\frac{\partial}{\partial t} = 2\pi f$. We then get.

$$p'(\mathbf{x},t) \quad \propto \quad \rho_\infty u_q^2 \frac{l_q}{|\mathbf{x}|}\left(\frac{l_q^2}{a_\infty^2}(2\pi f)^2 + \frac{2l_q^2}{a_\infty|\mathbf{x}|}(2\pi f) + \frac{2l_q^2}{|\mathbf{x}|^2}\right) \tag{A.32}$$

Inserting the lower frequency limit 500 [Hz] gives that the dominating term is the first term.

$$p'(\mathbf{x},t) \propto \rho_\infty u_q^2 \frac{l_q}{|\mathbf{x}|}Ma_q^2 \tag{A.33}$$

Appendix B

Errors related to compressible effects

The following derivation origins from the book, Physical Fluid Dynamics, by Tritton [60]. For high Reynold's number flows and in the absence of body forces, the incompressible momentum equation states that

$$\rho\frac{\partial u_i}{\partial t} + \rho u_j\frac{\partial u_i}{\partial x_j} \approx -\frac{\partial p}{\partial x_i} \tag{B.1}$$

The pressure gradient term can then be balanced by the convective term

$$\rho u_j\frac{\partial u_i}{\partial x_j} \sim \frac{\partial p}{\partial x_i} \tag{B.2}$$

or by the rate of change term

$$\rho\frac{\partial u_i}{\partial t} \sim \frac{\partial p}{\partial x_i} \tag{B.3}$$

or both. If variations predominantly occur in the x_1 direction, Eqs. B.2 and B.3 reduce to

$$\rho u_1\frac{\partial u_1}{\partial x_1} \sim \frac{\partial p}{\partial x_1} \tag{B.4}$$

and

$$\rho\frac{\partial u_1}{\partial t} \sim \frac{\partial p}{\partial x_1} \tag{B.5}$$

For both situations, the error will be of same magnitude, which will now be shown. Starting with a steady flow where the pressure gradient is balanced by the convective term, the left hand side of Eq. B.4 can be rewritten as

$$\rho \frac{\partial {u_1}^2}{\partial x_1} = 2\rho u_1 \frac{\partial u_1}{\partial x_1} \tag{B.6}$$

which gives that $u_1 \frac{\partial u_1}{\partial x_1} = \frac{1}{2} \frac{\partial (u_1)^2}{\partial x_1}$ and Eq. B.4 can then be rewritten as

$$\frac{\partial p}{\partial x_1} \sim \frac{1}{2} \rho \frac{\partial (u_1)^2}{\partial x_1} \tag{B.7}$$

If differences in pressure, Δp, and velocity, $\Delta {u_1}^2$, exist between two points separated by distance L, Eq. B.7 can be estimated to

$$\frac{\Delta p}{L} \sim \rho \frac{(\Delta u_1)^2}{L} \tag{B.8}$$

Further, if the difference in velocity, Δu_1, can be replaced by a characteristic velocity scale, U, an order of magnitude estimate for the pressure difference can be obtained

$$\Delta p \sim \rho U^2 \tag{B.9}$$

For weakly compressible flows, the density can be linearized to $\rho = \rho_\infty + \Delta\rho$ and the effect of compressibility, β, relating density and pressure can be expressed as

$$\frac{\Delta \rho}{\rho} \sim \beta \Delta p \tag{B.10}$$

By using the definition of the speed of sound under constant entropy, $a^2 = \frac{\partial p}{\partial \rho}|_s$, an order of magnitude for the speed of sound can be obtained by using Eq. B.10

$$a^2 \sim \frac{1}{\beta \rho} \tag{B.11}$$

Combining Eqs. B.11, B.10 and Eq. B.9 gives the final expression

$$\frac{\Delta \rho}{\rho} \sim \frac{\Delta p}{a^2 \rho} \sim \frac{U^2}{a^2} \tag{B.12}$$

The errors involved in considering the flow field to be incompressible are thus in the order of Ma^2. The result will be the same if instead the pressure gradient is balanced by the rate of change term, e.g. Eq. B.5. An estimate of the time scale is that $\frac{\partial}{\partial t} \sim \frac{U}{L}$, which gives

$$\frac{\Delta p}{L} \sim \rho \frac{U^2}{L} \tag{B.13}$$

This result is similar to that of Eq. B.9, and the error will be of a similar magnitude as for a convective dominated flow.

Papers